

OPTICAL SYSTEM DESIGN, INTEGRATION AND TESTING OF A 2D
SCANNING LIDAR

A THESIS SUBMITTED TO
THE GRADUATE SCHOOL OF NATURAL AND APPLIED SCIENCES
OF
MIDDLE EAST TECHNICAL UNIVERSITY

BY
KÜBRA CERİT

IN PARTIAL FULFILLMENT OF THE REQUIREMENTS
FOR
THE DEGREE OF MASTER OF SCIENCE
IN
PHYSICS

JANUARY 2022

Approval of the thesis:

**OPTICAL SYSTEM DESIGN, INTEGRATION AND TESTING OF A 2D
SCANNING LIDAR**

submitted by **KÜBRA CERİT** in partial fulfillment of the requirements for the
degree of **Master of Science in Physics, Middle East Technical University** by,

Prof. Dr. Halil Kalıpçılar
Dean, Graduate School of **Natural and Applied Sciences**

Prof. Dr. Seçkin Kürkçüoğlu
Head of the Department, **Physics**

Assist. Prof. Dr. Alpan BEK
Supervisor, Physics, **METU**

Examining Committee Members:

Assoc. Prof. Dr. Emre Yüce
Physics, METU

Assoc. Prof. Dr. Alpan Bek
Physics, METU

Assist. Prof. Kamil Çınar
Physics, Gebze Technical University

Date: 20.01.2022

I hereby declare that all information in this document has been obtained and presented in accordance with academic rules and ethical conduct. I also declare that, as required by these rules and conduct, I have fully cited and referenced all material and results that are not original to this work.

Name Last name: Kübra Cerit

Signature:

ABSTRACT

OPTICAL SYSTEM DESIGN, INTEGRATION AND TESTING OF A 2D SCANNING LIDAR

Cerit, Kübra
Master of Science, Physics
Supervisor: Assoc. Prof. Dr. Alpan BEK

January 2022, 102 pages

In this thesis, optical system design, integration and testing of a compact LIDAR system with 270 degree field-of-view that based on time of flight principle is developed by Rekrom Optoelectronics. This system can identify objects and measure distances up to 100 m away.

LIDAR has become a much needed and used technology in various fields. The most important of these areas are robotic systems, autonomous vehicles and unmanned aerial, land and sea platforms navigation and environmental awareness. The main reason that the LIDAR has become preferred technology is that it is much faster in the aspect of environmental awareness whereas being able to easily provide the distance information of the objects. LIDAR can provide high-resolution vision by generating millions of data points in real-time. This creates a precise map of the ever-changing surroundings that allow the objects to be recognized and categorized. And thanks to the advent and adoption of solid-state technology, the cost of these high-resolution sensors has also been considerably reduced, making them a perfect fit for a wide range of technologies.

Keywords: LIDAR, Light Detection and Ranging, Scanning LIDAR, Proximity Sensor

ÖZ

2 BOYUTLU TARAMALI LIDAR OPTİK SİSTEM TASARIMI, ÜRETİMİ VE TESTİ

Cerit, Kübra
Yüksek Lisans, Fizik
Tez Yöneticisi: Assoc.Prof. Dr. Alpan Bek

Ocak 2022, 102 sayfa

Bu tezde, Rekrom Optoelektronik tarafından, uçuş süresi prensibine dayalı, 270 derecelik görüş alanına sahip kompakt bir LIDAR sisteminin optik sistem tasarımı, entegrasyonu ve testi çalışmaları gerçekleştirilmiştir. Bu ürün nesneleri 100 m menzile içerisinde tanımlayabilir.

LIDAR, çeşitli alanlarda çok ihtiyaç duyulan ve kullanılan bir teknoloji haline gelmiştir. Bu alanların en önemlileri robotik sistemler, otonom araçlar ve insansız hava, kara ve deniz platformları navigasyon ve çevre bilincidir. LIDAR'ın tercih edilen bir teknoloji haline gelmesinin temel nedeni, nesnelerin mesafe bilgilerini kolaylıkla sağlayabilmesi ve çevre bilinci açısından çok daha hızlı olmasıdır. LIDAR, gerçek hayatta milyonlarca veri noktası üreterek yüksek çözünürlüklü görüş sağlayabilir. Bu, nesnelerin tanınmasına ve sınıflandırılmasına izin veren sürekli değişen çevrenin kesin bir haritasını oluşturur. Katı hal teknolojisinin gelişi ve benimsenmesi sayesinde, bu yüksek çözünürlüklü sensörlerin maliyeti de önemli ölçüde azaltılarak onları çok çeşitli teknolojiler için mükemmel bir uyum haline getirmiştir.

Anahtar Kelimeler: LIDAR, Işık Algılama ve Mesafe Ölçme, Taramalı LIDAR, Yaklaşım Sensörü

To my dear mom

ACKNOWLEDGMENTS

I would like to thank to my supervisor Assoc. Prof. Dr. Alpan Bek for his support, advice, and encouragement throughout the research.

I would also like to thank Assoc. Prof. Dr. Serhat akır who is one of the most valuable professor of the physics department of METU and always supports me under all circumstances.

I would also like to thank my colleagues especially Mustafa Kara, Barış Evran and my General Manager Altuğ Uar for his support and guidance in my study.

I would also like to thank my former colleagues Parisa Sharif, Muammer Kozan, Arash Badamchi, and Ercan Karagz for their moral support and endless patience.

I'm also grateful to my friends Aslı Papurcu, Onur Sevim, Elif Ekebař, Selen Yksel, and Melis Gelge for helping me to overcome obstacles in my life during this study.

I would also like to thank my family for their love and support throughout all my life.

This work is funded by Rekrom Optoelectronics.

TABLE OF CONTENTS

ABSTRACT.....	v
ÖZ	vi
ACKNOWLEDGMENTS	viii
TABLE OF CONTENTS.....	ix
LIST OF TABLES	xii
LIST OF FIGURES	xiii
LIST OF ABBREVIATIONS.....	xvi
CHAPTERS	
1 INTRODUCTION	1
1.1 Measurement Techniques with Light.....	2
1.1.1 Optical Triangulation	2
1.1.2 Phase Change	4
1.1.3 Time of Flight	5
1.1.4 Comparison of Various Distance Measurement Techniques	6
1.2 LIDAR Types	7
1.3 General Optical Definitions	10
1.3.1 Beam Divergence	10
1.3.2 Spot Diagram	11
2 LASER POWER CALCULATIONS	13
2.1 Source (Transmitter)	14

2.1.1	Rectangular Pulse	14
2.1.2	Gaussian Pulse	15
2.1.3	Negative Parabolic Pulse	15
2.1.4	Types of Transmitter Lasers	17
2.2	Atmospheric Transmission	19
2.2.1	Elder – Strong - Langer Method.....	24
2.3	Target (Energy Density and Reflected from Target)	26
2.3.1	Intersection Areas in Symmetric Case	27
2.3.2	Intersection Areas in Asymmetric Case	31
2.3.3	Reflection Types.....	35
2.4	Detector Performance	39
2.4.1	Responsivity and Quantum Efficiency	40
2.4.2	NEP.....	41
2.5	Optical Power Calculation Algorithm/Laser Reflection Simulator	41
2.5.1	Input Forms	42
2.5.2	Analysis Forms	48
3	OPTICAL SYSTEM DESIGN	55
3.1	Transmitter Optical Design.....	55
3.2	Receiver Optical Design	65
4	OTHER SYSTEM COMPONENTS	69
4.1	Electronic Design.....	69
4.2	Mechanical Design	71
4.3	Software Design.....	72
5	TESTING AND ANALYSIS	73

5.1	Transmitter Optical Performance	73
5.1.1	Optical Components Effects on Power	80
5.1.2	Beam Divergence, Profile	81
5.2	Back Focal Length	84
5.3	Receiver Performance	86
6	CONCLUSION	89
APPENDICES		
A.	DATASHEET	95
REFERENCES		97

LIST OF TABLES

TABLES

Table 2.1 Wavelength Regions of Atmospheric Windows	22
Table 2.2 Types of Atmospheric Scattering	23
Table 2.3 Mass of Water Vapor in Saturated Air	25
Table 2.4 Constants for Atmospheric Windows.....	26
Table 2.5 Transmitters Properties.....	50
Table 2.6 Receivers Properties	51
Table 2.7 A1 – V1 Pair Performance	52
Table 3.1 Spot Size and Beam Divergence of the Design.....	62
Table 5.1 Repetition Rate– Average Output Power	74
Table 5.2 Operating Voltage – Average Output Power	77
Table 5.3 Pulse Width – Average Output Power	78
Table 5.4 Effect of Optical Components on Output Power.....	81
Table 5.5 Beam Divergence Results	84

LIST OF FIGURES

FIGURES

Figure 1.1. The Schematic Diagram of Optical Triangulation (adapted from [10]).	3
Figure 1.2. A Schematic of Phase Change Method	4
Figure 1.3. The Schematic Diagram of ToF	5
Figure 1.4. LIDAR Types	7
Figure 1.5. Scanning Methods [19].....	8
Figure 1.6. Schematic of Beam Divergence	10
Figure 1.7. Spot Diagram.....	11
Figure 2.1. Pulse Shapes (adapted from [25]).....	16
Figure 2.2. EEL Schematic	17
Figure 2.3. VCSEL Schematic.....	18
Figure 2.4. Transmittance at Sea Level	21
Figure 2.5. Intersection of the Target and Spot.....	28
Figure 2.6. Intersection of the Target and Spot.....	28
Figure 2.7. Intersection of the Target and Spot.....	29
Figure 2.8. Intersection of the Target and Spot.....	29
Figure 2.9. Intersection of the Target and Spot.....	30
Figure 2.10. Intersection of the target and spot.....	31
Figure 2.11. Intersection of the Target and Spot.....	31
Figure 2.12. Intersection of the Target and Spot.....	32
Figure 2.13. Intersection of the Target and Spot.....	32
Figure 2.14. Intersection of the Target and Spot.....	33
Figure 2.15. Intersection of the Target and Spot.....	33
Figure 2.16. Intersection of the Target and Spot.....	34
Figure 2.17. Intersection of the Target and Spot.....	34
Figure 2.18. Intersection of the Target and Spot.....	35
Figure 2.19. Reflection Types.....	36
Figure 2.20. Reflection Geometry	37

Figure 2.21. Phong Model	39
Figure 2.22. Main Form of The Software.....	42
Figure 2.23. Source Form	43
Figure 2.24. Source Atmosphere Form	44
Figure 2.25. Target Form.....	45
Figure 2.26. Receiver Atmosphere Form	46
Figure 2.27. Receiver Form.....	47
Figure 2.28. Target Analysis Form.....	48
Figure 2.29. Sensor Analysis Form	49
Figure 2.30. Photocurrent – Beam Divergence Graph	53
Figure 3.1. NSC Fast Axis Simulation	56
Figure 3.2. NSC Slow Axis Simulation.....	56
Figure 3.3. Detector View of Laser Diode	57
Figure 3.4. Detector View of Aspheric Design	58
Figure 3.5. Fast (Left) and Slow (Right) Axis of Laser Diode.....	58
Figure 3.6. Effect of the First Lens on Fast Axis	59
Figure 3.7. Effect of the First Lens on Slow Axis	60
Figure 3.8. Detector View	60
Figure 3.9. Fast Axis View of the Design	61
Figure 3.10. Slow Axis View of the Design.....	61
Figure 3.11. Detector View of the Design.....	62
Figure 3.12. Z Position of First Lens – Beam Divergence Graph	63
Figure 3.13. Z Position of Second Lens – Beam Divergence Graph	63
Figure 3.14. First Lens Aperture - Beam Power Graph	64
Figure 3.15. First Lens Aperture - Beam Power Graph	64
Figure 3.16. Receiver Optical Design	65
Figure 3.17. Spot Diagram of the Receiver	66
Figure 3.18. Transmitter - Receiver Design	67
Figure 3.19. Scanning System	67
Figure 3.20. Transmission Graph of the Window	68

Figure 4.1. Transmitter PCB	69
Figure 4.2. Receiver PCB	70
Figure 4.3. Optomechanical Design.....	71
Figure 4.4. Software Interface	72
Figure 5.1. Transmitter PCB	74
Figure 5.2. Average Output Power – Repetition Rate Graph	75
Figure 5.3. Average Output Power – Repetition Rate Graph	76
Figure 5.4. Average Output Power – Operating Voltage Graph.....	77
Figure 5.5. Average Output Power – Operating Voltage Graph.....	78
Figure 5.6. Average Output Power – Pulse Width Graph.....	79
Figure 5.7. Average Output Power – Pulse Width Graph.....	79
Figure 5.8. Set – Up for Output Power	80
Figure 5.9. Set – Up for Beam Divergence.....	82
Figure 5.10. Spot Sample.....	82
Figure 5.11. Spot Size – Target Distance Graph	83
Figure 5.12. BFL Set - Up	85
Figure 5.13. Back Focal Length – Receiver Signal Graph	86
Figure 5.14. Electronic Signal Set-up	87
Figure 5.15. Signal Power – Target Range Graph	87
Figure 6.1. Test Image	90
Figure 6.2. The Architectural Drawing.....	91
Figure 6.3. The Point Cloud Data	92
Figure 6.4. The Image of LIDAR	93

LIST OF ABBREVIATIONS

LIDAR	: Light Detection And Ranging
CCD	: Charge Coupled Device
ToF	: Time of Flight
FoV	: Field of View
OPA	: Optical Phase Array
MEMS	: MicroElectroMechanical Systems
EEL	: Edge Emitting Laser
VCSEL	: Vertical Cavity Surface Emitting Laser
LED	: Light Emitting Diode
NIR	: Near InfraRed
NEP	: Noise Equivalent Power
SNR	: Signal to Noise Ratio
APD	: Avalanche Photo Diode
IR	: InfraRed
PCB	: Printed Circuit Board
LASER	: Light Amplification by Stimulated Emission of Radiation

CHAPTER 1

INTRODUCTION

In this work, a two - dimensional scanning LIDAR has been developed. One of the most up-to-date technology topics is LIDAR.

LIDAR is a distance measurement technology. The earliest use of LIDAR was in the field of meteorology in the early 1960s [1]. It was quickly adopted in agricultural and archaeology research [2]. It can assist distinguish plant types and assess their growth statuses on agricultural robots and agricultural aircraft [3]. In archaeology, LIDAR is also highly beneficial. It can assist in the rapid and low-cost creation of a high-resolution dataset. The LIDAR information is simple to incorporate into a Geographic Information System and may be utilized for municipal statics and planning, as well as archeological site searches [4].

LIDAR has become more important in autonomous vehicles, such as self-driving automobiles, automated guided vehicles, and unmanned aerial vehicles (UAVs), in recent years. It can be used by autonomous vehicles to identify and avoid obstacles, recognize and track objects, and perform simultaneous localization and mapping (SLAM) [5] [6] [7]. The need for LIDAR is continuously expanding due to the advent of self-driving technology.

When a laser is used as a transmitter and a photodiode is used as a receiver, a circuit is used to count the time between the laser rays leaving the source, striking an object, and returning to the diode. The speed of light is used to calculate the distance of the object from the system. A two-dimensional picture can be created by collecting numerous points inside a given range of view. A dedicated laser power calculation scheme and a corresponding software is developed. Using this software, the components to be used in the system are selected. Optical system design of receivers and transmitters are built on a commercially available ray-tracing simulation tool.

Other system components (electronic, mechanical and software) design is also developed. Eventually, following the completion of the designs, the system is integrated and the performance of the system is evaluated.

1.1 Measurement Techniques with Light

There are mainly three techniques to measure distance with light. These are optical triangulation, phase change, and time of flight. The most fundamental and important difference between these three methods, while pulsed laser source is used in time of flight and optical triangulation technique, continuous-wave source is used in phase change method [8]. In the following section, these methods are described.

1.1.1 Optical Triangulation

Optical triangulation is an outdated method for determining object distance. This method has been used around the year 600 BC by the Greek mathematician Thales of Miletus in measuring the height of the Giza pyramids and determining the distance to a ship that was in the sea [9]. Laser triangulation is the other name for it. The displacement information of optical signals is converted to electrical signals using this approach.

The basic triangulation sketch with a single laser is shown in Figure 1.1. A typical direct laser triangulation optical system includes a laser transmitter, convergent and receiving lenses, a CCD linear array sensor, and a signal processing circuit [10]. Assume that the sensor's light spot irradiates on the surface of the measured item at position A, and that point B on the CCD imaging position is a reflecting spot. The displacement of the spot on the CCD image point is x' if the position of point A changes and the movement distance is x .

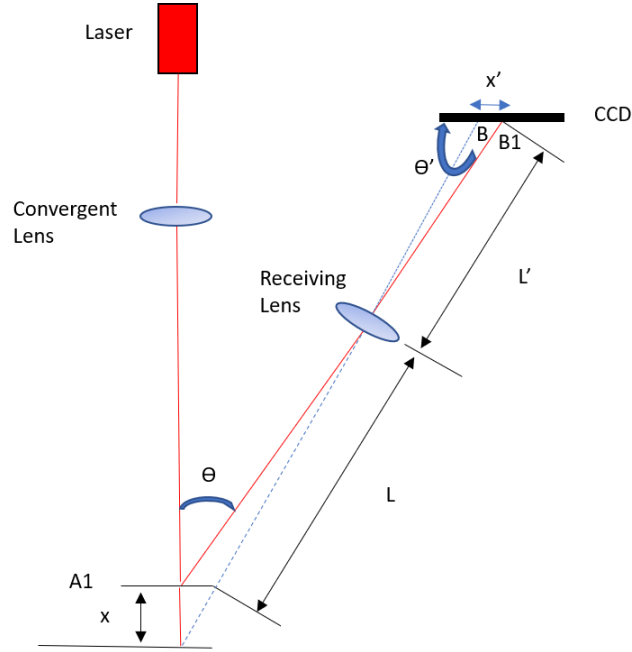


Figure 1.1. The Schematic Diagram of Optical Triangulation (adapted from [10])

The linear array of the CCD device, the laser transmitter axis, and the lens acceptance optical axis are all on the same plane. The measuring principle is as follows: the laser produces a parallel light beam that the condenser lens focuses on the object's surface. Due to diffuse reflection, the laser beam is then received by an imaging lens at a different angle and then on the sensitive surface where a spot forms. The location of the spot on the sensor varies when the position of the laser point changes due to the displacement of the object. The position of the laser point x on the surface of the measured object may be computed using the position of the spot x' by using the following trigonometric sine theorem:

$$x = \frac{L x' \sin \theta}{L' \sin \theta - x' \sin(\theta + \theta')} \quad (1)$$

In the formula, x is the object's movement distance, and x' is the image point's movement distance; θ is the angle between the incident beam and the receiving lens's axis; θ' is the angle between the surface of the photosensitive CCD receiving lens's axis; L is the receiving lens's object distance, which is the distance between point A

and receiver lens; L' is the distance between the surface of the photosensitive CCD receiving lens's axis.

The triangulation method is frequently used in a range of industrial applications. The length of the measurement varies from a few millimeters to several meters. This technique suffers from the missing part problem, which means that the receiver cannot always see what the source beam is lighting.

1.1.2 Phase Change

In this method, distance is calculated by a sinusoidal signal sent to the target. The phase difference between the reference signal and the target is measured by detecting the reflected laser energy on the target. A diagram of the phase change technique is shown in Figure 1.2.

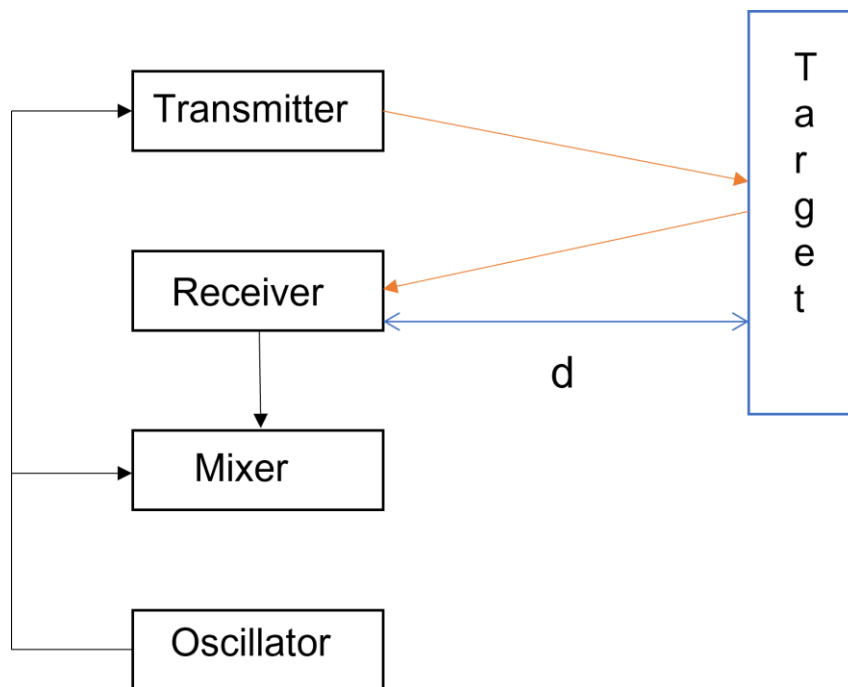


Figure 1.2. A Schematic of Phase Change Method

The phase difference in a system with a modulation frequency of f_0 , a target distance of d , and an ambient refraction index of n may be computed using the equation below [11].

$$\Delta\phi = 4\pi n f_0 d / c \quad (2)$$

The following equation expresses the relationship between the target distance and the phase difference.

$$d = c\Delta\phi / 4\pi n f_0 \quad (3)$$

1.1.3 Time of Flight

In a variety of LIDAR applications, ToF (Time of Flight) has become a significant depth-sensing method [12]. ToF laser distance measurement technique based on semiconductor pulsed laser diodes. Laser diodes provide a steady, long-life, and high repetition rate pulse. As compared to alternative methods that use a continuous laser source, accurate and quick distance measurements may be achieved.

In this method, a high precision counter is used to measure the time between the transmitted and received of a laser pulse, as seen in Figure 1.3.

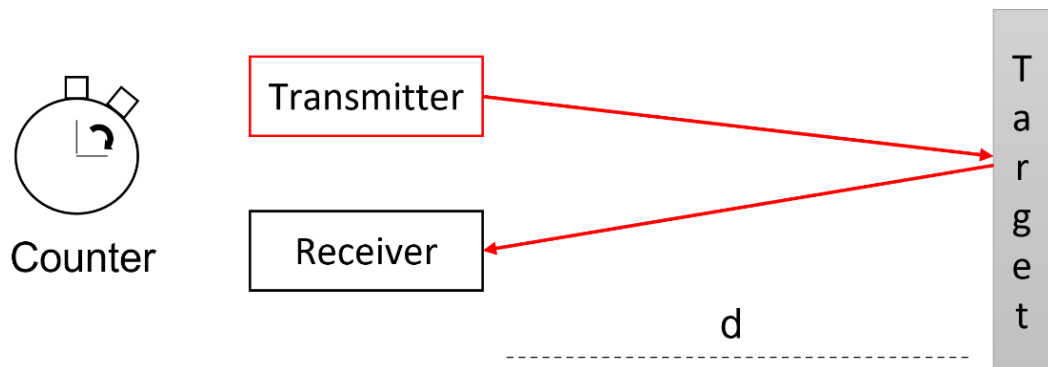


Figure 1.3. The Schematic Diagram of ToF

Typically, measuring begins with the laser pulse's emission and ends with the first detected photon. The receiver collects pulses from the laser source after they have reflected from the target. The laser pulse travels twice the distance between the source and the target. The laser travels at the speed of light, therefore calculating the distance to the target is as simple as applying the following formula:

$$d = \frac{c \cdot t}{2} \quad (4)$$

In the formula, d is the distance between the transmitter and target, t is the total time of flight of the laser pulse, and c is the speed of light in the medium.

1.1.4 Comparison of Various Distance Measurement Techniques

Three techniques that are mentioned above are analyzed. When comparing accuracy, it can be seen that the optical triangulation technique's accuracy reduces as the distance rises. At distances of less than 10 meters, this approach allows for precise measurements. In the case of ToF technique, this situation is the opposite. This technique can measure large distances with great precision.

For objects with high surface reflectivity, distance measuring with an accuracy of a few millimeters can be obtained using the phase change approach. However, there is a significant performance decrease on surfaces with poor reflectivity. The phase difference measurement accuracy is correlated with the signal-to-noise (SNR), hence the phase change method is often utilized at distances of a few millimeters to ten meters.

In addition to these, the ToF technique allows us real – time image creation.

As a result of all these comparisons, it has been determined that the TOF approach will be used in the LIDAR that will be developed.

1.2 LIDAR Types

According to how they scan the laser beam, LIDAR may be classified. LIDARs are divided into two as scanning and non – scanning as shown in the Figure 1.4 [13].

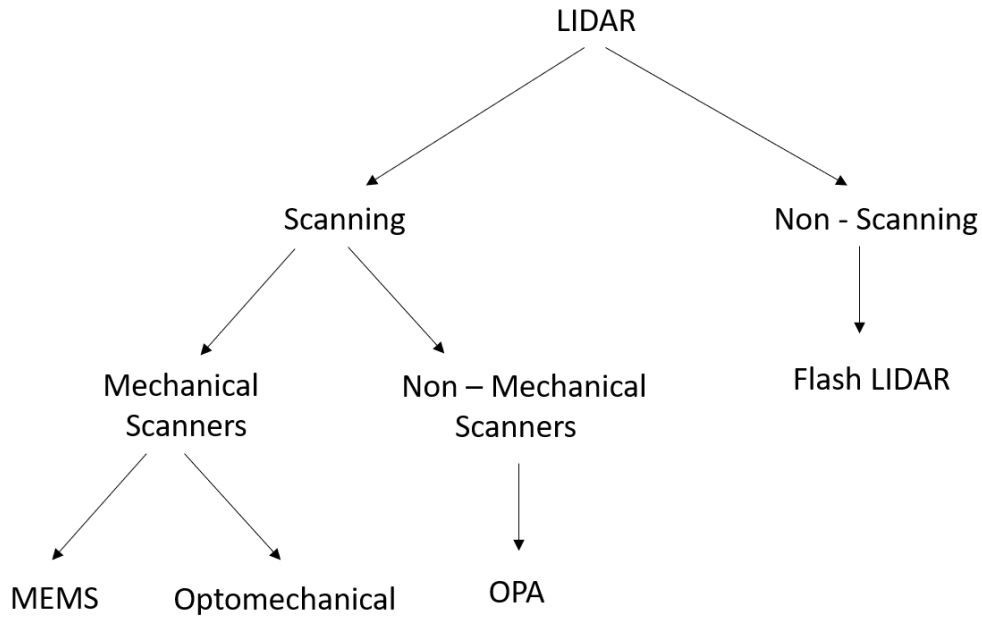


Figure 1.4. LIDAR Types

Flash LIDAR is the most widely used non-scanning LIDAR type [12]. In this type of LIDAR, the laser source illuminates the whole FoV while an array of photodetectors at the same time takes up the ToF information of individual pixels in the FoV [13] [14]. Because each pixel of the photodetector array gets just a small fraction of the returned laser light, the signal-to-noise ratio which limits the distance measuring range or needs high laser power is poor [12] [15]. In addition to this, there is no moving parts.

Non – mechanical scanning systems are also called solid-state scanners because there is no moving parts [15]. Optical phased arrays are a type of solid-state beam steering technology that allows optical beams to be steered non-mechanically [16]. The laser power is divided into an array of transmitters, each with its own phase control. A

laser beam may be created and guided by dynamically altering the relative phase shifts among the transmitters [17].

Mechanical Scanning LIDAR is also divided into two: MEMS scanners and optomechanical scanners. MEMS mirrors can steer, modify, and switch light as well as regulate phase. Only the small mirror plate (with a diameter of 1–7 mm) of the MEMS device moves in the design of a MEMS mirror-based LIDAR, while the rest of the system components remain immobile. They are also called quasi-static-state LIDAR.

The most prevalent form of LIDAR scanner is the optomechanical scanner [18]. The scanning methods used in LIDARs differ depending on the changes such as flight route, flight speed, scanned geography, and target, as seen in Figure 1.5.

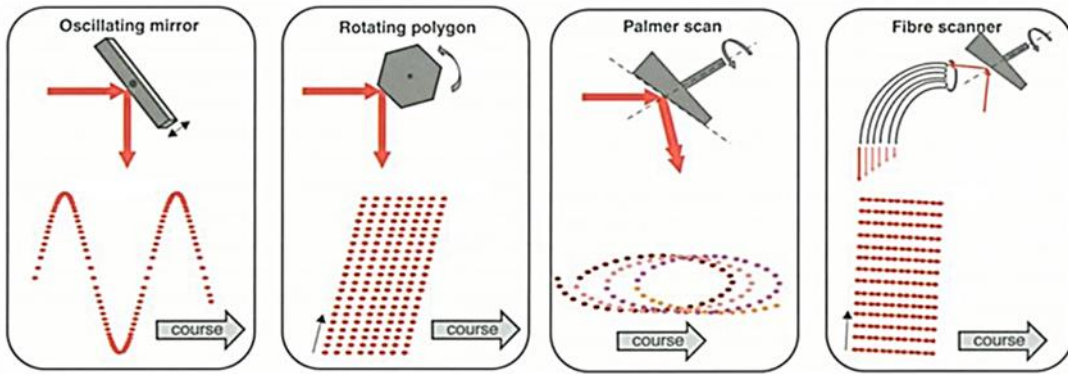


Figure 1.5. Scanning Methods [19]

The oscillating mirror scanning technique is based on the single axis scanning principle. Scanning on a second axis can only be achieved with the direction of movement of a moving platform. For this reason, mounting this type of mechanism on a moving platform is essential for the system to scan in two axes. The biggest advantage of the oscillating mirror scanning technique is to focus on the desired area by changing the scanning angle and oscillation speed of the mirror used.

The rotating polygon scanning technique is scanning by rotating the mirrors arrayed on the surfaces of a polygon on a single axis. As in the oscillating mirror technique, the second axis is scanning in the direction of movement of the platform. The

disadvantage is that the scan angle is fixed as it is determined by the surface dimensions of the polygon.

Quasi scanning technique has a nonlinear scanning model. The angled mirror or mirrors cause the laser beam to produce an ellipse-like shape. This pattern allows the laser to scan certain areas of the surface twice. It is generally used for mapping areas with dense vegetation and searching for an object in forested terrain. The feature of scanning the same area twice reduces the occupancy rate in the scanned scene by overlapping the laser point clouds. Since the size of the scanning axis depends on the angle of the mirror, it can scan independently of the movement direction of the platform.

The fiber scanning method consists of two fiber bundles, a laser transmitter, and a receiver. The number of arrayed fibers at the laser emitting end of the fiber bundle determines an axis of the scanned area and is constant. The other axis is determined by an oscillating mirror depending on the oscillation angle. This gives the ability to scan in both axes independent of the movement direction of the platform, like quasi scanning in fiber scanning method.

It should be stated that the most important design parameter in LIDAR design is the appropriate choice of the applied laser and its power which includes analytical approaches to the illumination pattern on the target, the target reflectance, and the signal-to-noise expected from the detector side. Hence, I dedicate the second chapter to discuss the details grounding the choice of the laser power. In the third chapter, I present optical system design. In the fourth chapter, I present other system components such as control electronics, mechanical frame and software. In the fifth chapter, I present the test results and performance benchmarks. In the last chapter, I conclude with my discussions of the 2D LIDAR system as a whole.

1.3 General Optical Definitions

1.3.1 Beam Divergence

After exiting the source, laser beams expand and propagate. The amount of this expansion in angles is expressed in terms of the beam divergence [20]. This behavior is exemplified in Figure 1.6.

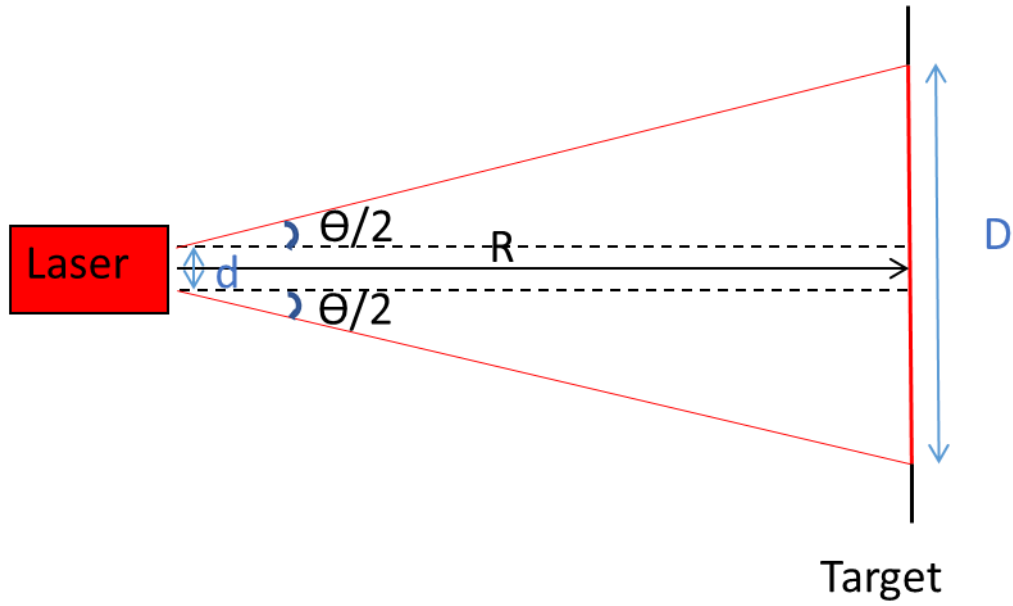


Figure 1.6. Schematic of Beam Divergence

As seen in the figure, the beam exits the source with the diameter d and reaches the diameter D after exceeding the distance R . The amount of expansion in diameter is denoted by θ . This angle known as beam divergence, and it is calculated by measuring the spot diameter and using equation that is given below:

$$\tan(\theta/2) = (D/2 - d/2)/R \quad (5)$$

1.3.2 Spot Diagram

The rays coming from a dimensionless point transform into a two-dimensional shape after passing through the optical system [21]. This shape and size (geometric diameter) give information about the optical performance of the system. The spot diagram of an exemplary optical system is given in Figure 1.7.

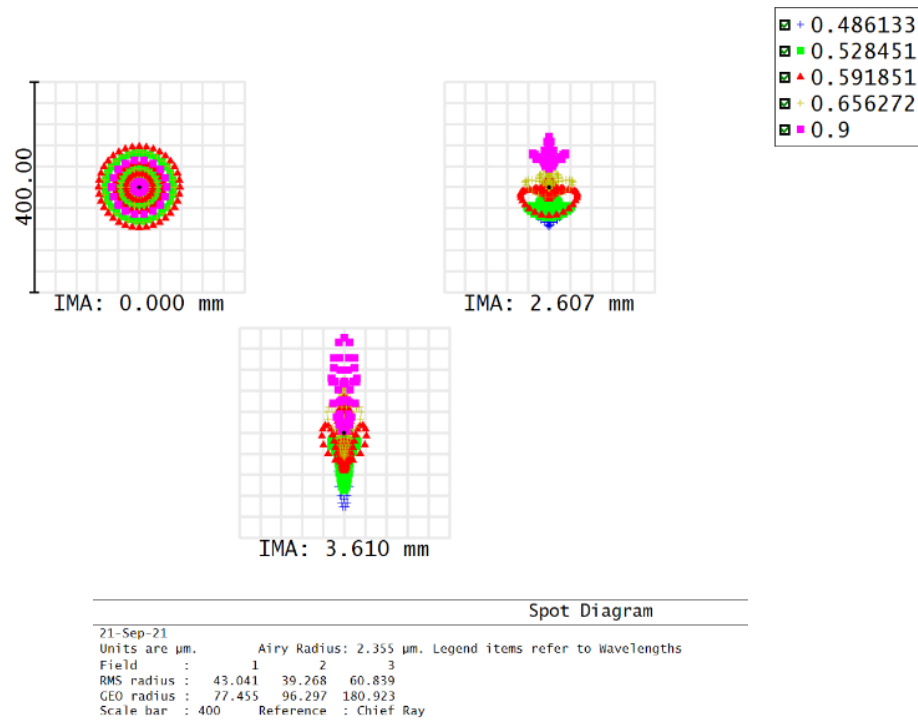


Figure 1.7. Spot Diagram

Spot diagram gives us the RMS radius value. RMS radius is the best representation of infinitely many rays. Therefore, if the RMS radius is within the airy disc, then the represented system must be successfully focused.

Diffraction at the edge of a circular aperture produces an airy disc pattern, which consists of a center core of light surrounded by concentric rings of gradually decreasing intensity.

CHAPTER 2

LASER POWER CALCULATIONS

For laser systems, the most difficult part of evaluating their performance is determining how much optical power is available at the receiver's aperture [24]. Under certain conditions and against a given target, a laser range equation is used to calculate how much power will be received by the laser beam. For performance analysis of these systems, special situations such as atmospheric propagation, reflection characteristics of the target, and detection performance must be evaluated.

A laser beam is generally weakened as it travels through the atmosphere. Furthermore, the beam is frequently widened, defocused, and even diverted from its initial propagation path. When operating at a specific wavelength, the output power and atmospheric conditions determine the degree of attenuation and beam distortion. The effects have a linear behavior when the output power is low. Absorption, scattering, and atmospheric turbulence are examples of these linear effects. However, if the power is large enough, additional effects emerge, which are characterized by non-linear interactions such as thermal blooming, kinetic cooling, bleaching and atmospheric breakdown [25]. Regardless of the situation, atmospheric factors can have a major impact on the beam's effectiveness.

Another essential part of the laser system performance evaluation is the understanding of target reflection characteristics. It is possible to define a reflection characteristic of the surface in two different ways: by using the specular component and the diffuse component [26]. The energy reflected away from the surface at an opposite angle of incidence is known as the specular component. On the other hand, diffusive or Lambertian energy reflects in all directions with highest along normal to the target surface and decreases as a function of cosine of the angle off normal to target surface.

The general laser range equation is given below [27]:

$$P_R = \frac{4P_t}{\pi(\theta_t)^2 R^2} \frac{A_{tr}}{\Omega_{tr} R^2} \frac{\pi D^2}{4} \rho_{tr} T_{atm}^2 T_o \quad (6)$$

In the formula, P_R is the signal power at the receiver (W), P_t is the transmitter pulse power (W), θ_t angular beam divergence of transmitted beam (rad), R is the range between LIDAR and the target (m), ρ_{tr} is the target surface reflectance, A_{tr} is the target surface area (m²), Ω_{tr} is the solid angle of dispersed radiation (steradian), D is the diameter of circular receiver aperture (m), T_{atm} is the atmospheric transmission and T_o is the optical transmission.

In this chapter, laser systems performance analysis is discussed in terms of system requirements, air propagation and target reflection characteristics, as well as some basic theoretical background.

2.1 Source (Transmitter)

The form of the pulse delivered to the target surface is determined by the power generated by the laser source. The three widely used pulse models are Gaussian, square and negative parabolic [25].

2.1.1 Rectangular Pulse

The simplest waveform model is the rectangular pulse shape [25]. The rectangular pulse model simulates laser pulses by using an approximation of their real form. The quantity of energy per unit time in this model provided by,

$$P_t(t) = \frac{E_t}{p_w} \times \text{rect}\left(\frac{t}{P_t}\right) \quad (7)$$

where P_t is the power of the laser pulse as a function of time, E_t is the amplitude of the pulse in joules, t is the duration in seconds, and p_w is the pulse width from edge to edge in seconds.

2.1.2 Gaussian Pulse

The Gaussian pulse shape is the first nonrectangular pulse shape, and its function is the same as that of a normally distributed random variable's probability density function [25]:

$$P_t(t) = \frac{E_t}{\sigma_w \sqrt{2\pi}} e^{\frac{-t^2}{2\sigma_w^2}} \quad (8)$$

The width of the Gaussian pulse shape in seconds is represented by σ_w in this equation. Gaussian pulse model gives a more realistic representation of the power than the rectangular pulse because transmitter power is a constant function of time. The Gaussian model has one weak point: when the pulse power continues endlessly in the negative direction, it is not zero, even though it is extremely close [29]. This contrasts with the case when the laser pulse strength is zero prior to firing.

2.1.3 Negative Parabolic Pulse

In this model, the laser power is represented as a negative parabola in time. The negative parabola model, the pulse is expressed by the following equation [25]:

$$P_t(t) = \frac{3E_t}{2p_w} \left(1 - \frac{4t^2}{p_w^2} \right) \text{rect}\left(\frac{t}{p_w}\right) \quad (9)$$

where p_w is the pulse width. This function's scaling ensures that the pulse's energy is equal to the variable E_t .

The negative parabolic pulse model overcomes the Gaussian model's problem of power dissipation in the negative direction. In the model, the pulse power is zero while approaching to infinity in a negative direction. In contrast, this model does not accurately represent the trend (tendency) that the real pulse power exhibits when it approaches infinity in a positive direction. In Figure 2.1, these three pulse models are compared.

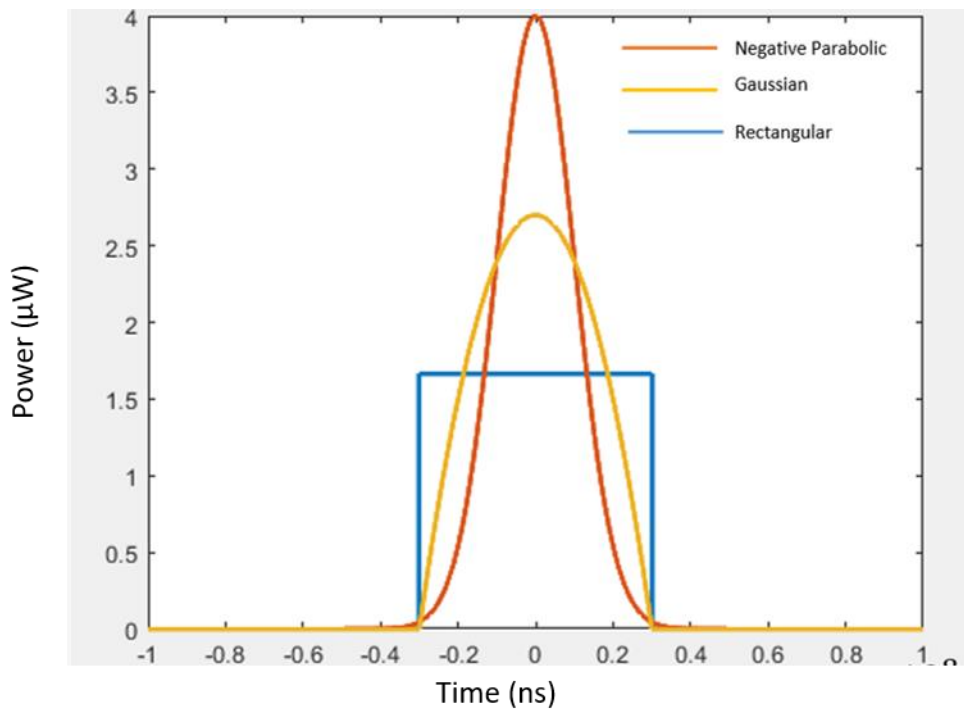


Figure 2.1. Pulse Shapes (adapted from [25])

In the figure, each pulse has a total of 1 J of energy and a total width of 6 ns [25]. As shown in the figure, negative parabolic pulse has the highest power under same circumstances.

2.1.4 Types of Transmitter Lasers

In this part of the thesis, market research was conducted for the source to be used in the product. First, theoretical knowledge was obtained about the light sources used in LIDAR systems, and then a comparison has been made.

Mainly, there are two types of diode laser. They are EEL (Edge – Emitting Laser) and VCSEL (Vertical Cavity Surface Emitting Laser).

The original semiconductor laser concept and a mature technology that has been utilized for decades is the edge-emitting laser. As shown in the Figure 2.2, light propagates in a waveguide structure parallel to the semiconductor surface and is emitted from the edges of the semiconductor chip [26].

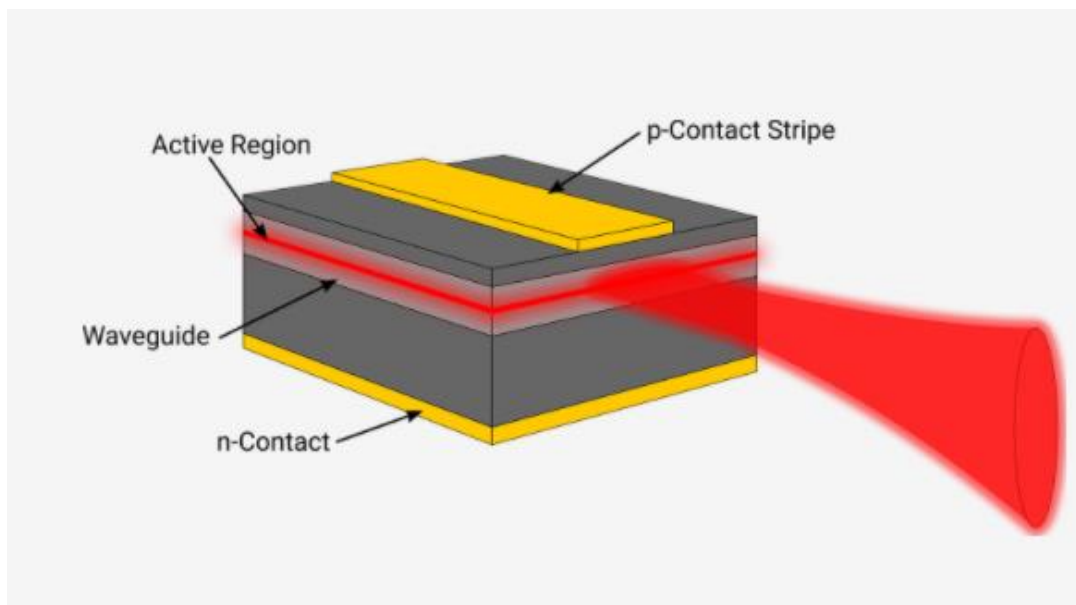


Figure 2.2. EEL Schematic

In this structure, this chip operates as a cavity mirror. High gain is achieved thanks to the active zone varying between micrometers and millimeters. Thus, high output power can be achieved.

Comparison to the edge emitting laser, VCSEL is a new technology [27]. As shown in the Figure 2.3, In the vertical cavity surface emitting lasers, light propagates perpendicular to the semiconductor surface.

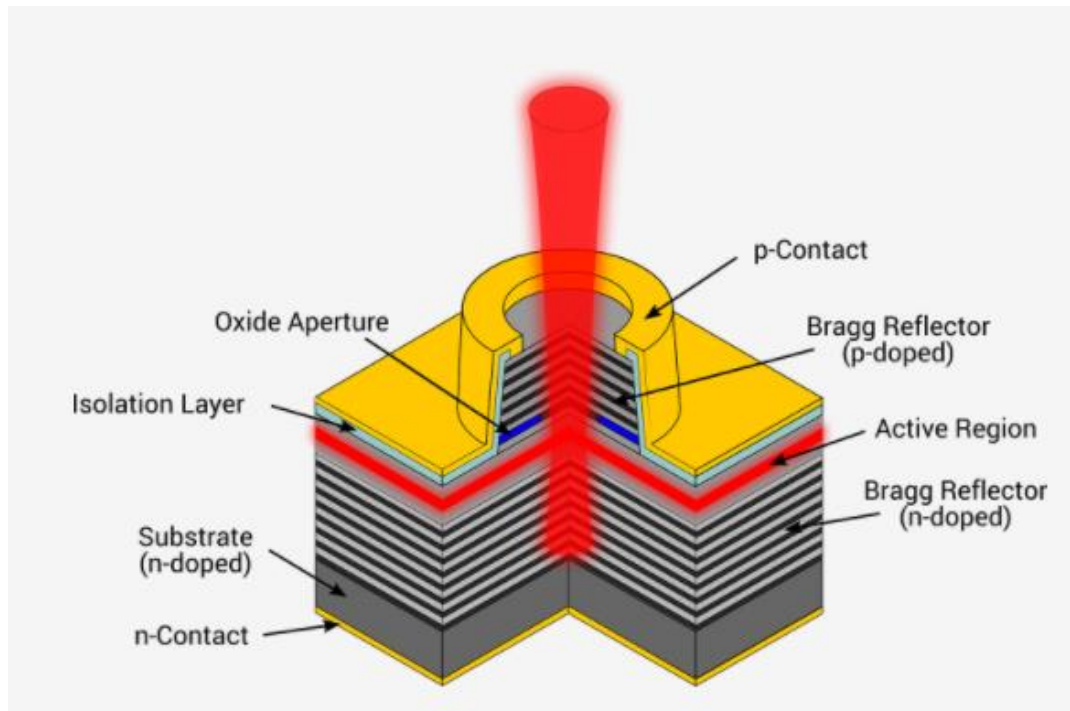


Figure 2.3. VCSEL Schematic

The vertical cavity is obtained by two bragg reflectors that have different refractive indices materials. Gain is provided by electrically pumped quantum wells or quantum dots located in the active region between the monolithically grown semiconductor mirror, leading to single – longitudinal mode operation [31]. Confining both current and optical field by oxide apertures enables operation in single – transverse mode, making the VCSEL compact and efficient source of laser emission with excellent beam quality [31].

There are some advantages of VCSEL when comparing to the EEL. The biggest advantage of VCSEL is that can be tested in wafer level [32]. A finished wafer may be checked in a wafer probe machine, which uses microscopic electrical probes to contact each device and apply current. If it's excellent, it can be measured using a camera. As a result, excellent devices may be recognized before the wafer is sliced,

and poor ones can be tagged for disposal automatically. This eliminates the need to dice and mount a VCSEL in order to test it, saving time and money. The other advantage of VCSEL is output beam quality. Although the beam is homogeneous, the beam divergences are larger than the emitting laser.

Although VCSEL seems has many advantages, it was decided to use EEL in this project because VCSEL is an emerging technology. Edge emitting lasers dominate the market because of the maturity of the technology, high power & cost efficient.

2.2 Atmospheric Transmission

Characterizing and modeling the effects of linear and non-linear air propagation on laser beams has been the subject of several studies. Only a basic introduction to the principles of laser beam propagation is given in the next paragraphs, with a focus on the processes that impact peak irradiance at the target.

The Beer's Law describes the attenuation of laser radiation in the atmosphere [22]:

$$T = I(z)/I_0 = e^{-\gamma z} \quad (10)$$

In the equation, τ is the transmittance, γ is the attenuation coefficient, and z is the length of the transmission path. If the attenuation coefficient varies with the path,

$$T = e^{-\int_0^z \gamma(z) dz} \quad (11)$$

Molecular absorption, molecular scattering, aerosol absorption, and aerosol scattering are the four processes that define the attenuation coefficient [29]. Then the coefficient is:

$$\gamma = \alpha_m + \beta_m + \alpha_a + \beta_a \quad (12)$$

where α is the absorption coefficient, β denotes the scattering coefficient, and m and a denote the molecular and aerosol processes, respectively. The wavelength of the laser light affects the coefficients in the equation.

Sometimes it's easier to talk about absorption and scattering in terms of the individual particles' absorption and scattering cross sections (a and s , respectively):

$$\alpha = \sigma_a N_a \quad (13)$$

$$\beta = \sigma_s N_s \quad (14)$$

In these equations, the concentrations of absorbers and scatterers are represented by N_a and N_s , respectively.

The atmosphere includes finely distributed solid and liquid particles (of ice, dust, aromatic and organic substances) that range in size from a cluster of a few molecules to particles with a radius of roughly 20 μm in the absence of precipitation. Larger particles stay in the air for a short period and are only detected near to their sources. The term "aerosol" refers to a colloidal system in which a continuous medium (in this example, air) is used to disperse solid or liquid particles. The size, chemical content, and concentration of aerosol particles all effect the attenuation coefficients. These particles are often thought to be homogenous spheres with two parameters: radius and index of refraction. The index of refraction is complicated in general. Thus, it can be written as;

$$\hat{n} = n - ik = n \left(1 - i \frac{k}{n} \right) = n (1 - i\kappa) \quad (15)$$

In the equation, n is the real part and k is the imaginary part. $\kappa = k/n$ is the extinction coefficient. The absorption is calculated using the imaginary component. The

absorption constant is referred to as k that is related to the absorption coefficient α .

$$\alpha = 4\pi f k / c \quad (16)$$

where c is the speed of light in a vacuum and f is the incoming radiation's frequency. The main atmospheric absorbers for the wavelength range of higher interest in laser beam propagation (the visible area to about 15 μm) include water, carbon dioxide, and ozone molecules. Because these molecules preferentially absorb radiation by altering vibrational and rotational energy levels, attenuation occurs. Nitrogen (N_2) and oxygen (O_2), the two most abundant gases in the earth's atmosphere, are homonuclear, which means they don't have an electric dipole moment and hence don't have molecular absorption bands. Figure 2.4 depicts the air spectral transmittance (percentage) measured along a horizontal path of 1820 meters at sea level [30].

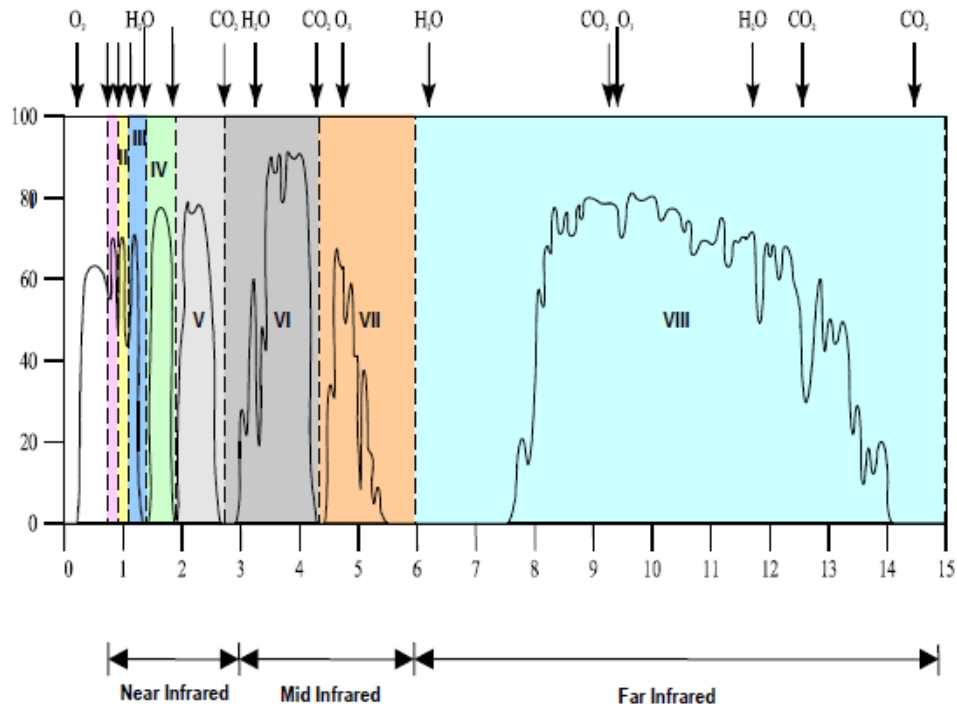


Figure 2.4. Transmittance at Sea Level

In the upper portion of the image, the chemical responsible for each absorption band is displayed. The most important absorbing molecules are undoubtedly H_2O and CO_2 . This is also true for the height range between sea level and roughly 12 kilometers. The concentration of H_2O varies between 10^{-3} and 1% depending on weather conditions, altitude, and geographic location. The concentration of CO varies between 0.03 and 0.04 percent.

Other absorbing molecules found in the atmosphere are methane (CH_4), with a concentration of around 1.5×10^{-4} percent; nitrous oxide (N_2O), with a concentration of around 3.5×10^{-5} percent; carbon monoxide (CO) with a typical concentration of 2×10^{-5} percent; and ozone (O_3), with a concentration as large as 10^{-3} percent at an altitude of around 30 km. Ozone concentrations around sea level are quite low. The wavelength intervals in Figure 2.4 where the transmittance is quite high are referred to as "atmospheric windows."

The laser wavelength must fall well inside one of these windows for effective energy transfer. Within a wavelength range of 0.72 to 15.00 μm , there are a total of eight such windows.

Table 2.1 Wavelength Regions of Atmospheric Windows

Window Number	Window Boundaries (μm)	
I	0.72	0.94
II	0.94	1.13
III	1.13	1.38
IV	1.38	1.90
V	1.90	2.70
VI	2.70	4.30
VII	4.30	6.00
VIII	6.00	15.00

The scattering coefficient β is also affected by the incident radiation's frequency, as well as the scattering particle's index of refraction and radius. Forced oscillations of the bound and free charges within the sphere are produced by the incident electromagnetic wave, which is considered to be a plane wave in a particular polarization state. These oscillating charges generate secondary fields both within and outside the sphere. The vector sum of the primary (plane wave) and secondary fields is the resultant field at any location. Following the determination of the resulting field, the scattering cross section is calculated using the following formula [31]:

$$\sigma_s = \frac{\text{total power scattered by the scatterer}}{\text{magnitude of time – averaged incident poynting vector}} \quad (17)$$

There is no energy loss in the scattering process, simply a directional redistribution, which might result in a considerable drop in beam intensity over long route lengths. The kind of scattering is determined, as shown in Table 2.2, by the physical size of the scatterer [36]. Rayleigh scattering occurs when air molecules with a diameter of several angstrom units collide, whereas Mie scattering occurs when aerosols collide. Furthermore, diffraction theory better describes the scattering process when the scatterers are quite big, such as water droplets observed in fog, clouds, rain, or snow.

Table 2.2 Types of Atmospheric Scattering

Type of Scattering	Size of Scatterer
Rayleigh Scattering	Larger than electron but smaller than λ
Mie Scattering	Comparable in size to λ
Non-selective Scattering	Much larger than λ

2.2.1 Elder – Strong - Langer Method

Elder and Strong [32] proposed and Langer refined a simple technique that yielded approximate values of the absorption coefficient. Their method is especially valuable since it allows them to relate the atmospheric transmission of the i th window to the relative humidity. Variability in transmission are thought to be driven by changes in the water content of the air. Variations in H_2O concentration induce changes in absorption, while changes in the size and quantity of droplets of water with humidity cause shifts in the scattered component. This is a reasonable guess since the influence of other atmospheric components on the transmittance of a particular atmospheric window is relatively constant. It is common to describe the number of H_2O molecules encountered by the light beam in terms of the number of precipitable millimeters of water in the route. The amount of precipitable water is defined as the depth of the layer of water created if all of the water molecules along the propagation route were condensed in a container with the same cross-sectional area as the beam. A cubic meter of air with an absolute humidity of gram per m^3 will produce condensed water across a $1 m^2$ area with a depth of:

$$w' = 10^{-3}\rho \quad (18)$$

w' is the precipitable water, which is measured in millimeters per meter of route length. For a z -meter-long path, the equation becomes

$$w = 10^{-3}\rho * z \quad (19)$$

w denotes the total amount of water that can be precipitated in millimeters. The density of water vapor, denoted by ρ , may be calculated by multiplying the relevant number in Table 2.3 by the relative humidity (RH).

Table 2.3 Mass of Water Vapor in Saturated Air

(°C)	Temperature									
	0	1	2	3	4	5	6	7	8	9
-20	0.89	0.81	0.74	0.67	0.61	0.65				
-10	2.15	1.98	1.81	1.66	1.52	1.40	1.28	1.18	1.08	0.98
-0	4.84	4.47	4.13	3.81	3.52	3.24	2.99	2.75	2.54	2.34
0	4.84	5.18	5.54	5.92	6.33	6.76	7.22	7.70	8.22	8.76
10	9.33	9.94	10.57	11.25	11.96	12.71	13.50	14.34	15.22	16.17
20	17.22	18.14	19.22	20.36	21.55	22.80	24.11	25.49	27.00	28.45
30	30.04	31.70	33.45	35.28	37.19	39.19				

The following equation [33] which is useful for computer code implementations, can be used to get similar numerical results:

$$\rho = 1322.8 \frac{RH}{T} \exp\left(\frac{25.22(T - 237.16)}{T} - 5.31 - \ln\left(\frac{T}{273.16}\right)\right) \quad (20)$$

In the equation, the relative humidity (as a percentage) is RH, while the absolute temperature is T (K). For every given value of the precipitable water content, the Elder Strong technique may be used to determine the absorptive transmittance T_{ai} for the i th window.

$$T_{ai} = e^{-A_i \sqrt{w}}, \text{ for } w < w_i \quad (21)$$

$$T_{ai} = k_i \left(\frac{w_i}{w}\right)^{\beta_i}, \text{ for } w > w_i \quad (22)$$

The values of these constants that is in the equations for atmospheric windows are listed in Table 2.4.

Table 2.4 Constants for Atmospheric Windows

Constants Window	A_i	k_i	β_i	w_i
I	0.0305	0.800	0.112	54
II	0.0363	0.765	0.134	54
III	0.1303	0.830	0.093	2.0
IV	0.211	0.802	0.111	1.1
V	0.350	0.814	0.1035	0.35
VI	0.373	0.827	0.095	0.26
VII	0.598	0.784	0.122	0.165

These equations and tables can be used to calculate the absorptive transmittance (T_{ai}) of laser beam wavelengths that fall inside certain atmospheric windows.

2.3 Target (Energy Density and Reflected from Target)

The light beam emitted from the transmitter, creates a spot on the target located at a certain distance. At the distance, this spot has optical power. Two situations should be considered at this point. Firstly, since the power coming out of the source is under influence of atmospheric effects, decrease occurs when it reaches the target. Secondly, there must be an intersection area, taking into account whether the spot is larger or smaller than the target.

Usually, since the target desired to be detected in laser systems is obvious, the dimensions of the target are known. The dimensions and shape of the spot formed at the target distance depend on the symmetric and asymmetric propagation of the transmitter. In symmetric propagation, beam divergence of vertical and horizontal directions are equal. In this case, spot becomes circular. In asymmetric propagation, vertical and horizontal beam divergences are not equal, so spot becomes ellipse.

In symmetric case, spot diameter can be calculated by using relation given below;

$$D = d + 2 \tan\left(\frac{\theta}{2}\right) R_1 \quad (23)$$

Variable in the equations (23), (24) and (25) are explained in the section 1.3.1.

In asymmetric case, vertical and horizontal spot diameter can be obtained by using relation given below;

$$D_x = d_x + 2 \tan\left(\frac{\theta_x}{2}\right) R_1 \quad (24)$$

$$D_y = d_y + 2 \tan\left(\frac{\theta_y}{2}\right) R_1 \quad (25)$$

For both cases, how to find the intersection areas in scenarios where the target is rectangular and circular is examined in the following headings.

2.3.1 Intersection Areas in Symmetric Case

In this section, spot is assumed to be circular. The cases where the target is circular and rectangular evaluated separately. In the following equations and figures, D_t is target diameter and D_s is the spot diameter.

2.3.1.1 Circular Target

The case where the spot diameter is larger than the target diameter is shown in the Figure 2.5.

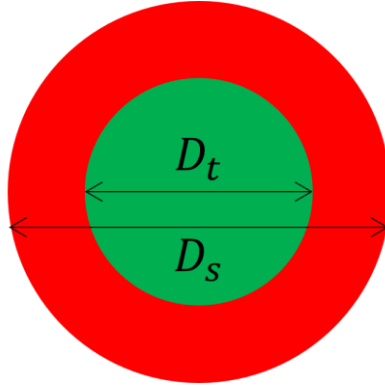


Figure 2.5. Intersection of the Target and Spot

In this situation, intersection area is target area itself. This area can be calculated by using

$$A_{intersection} = \pi D_t^2 / 4 \quad (26)$$

The other case where the spot diameter is smaller than the target diameter is also illustrated in Figure 2.6.

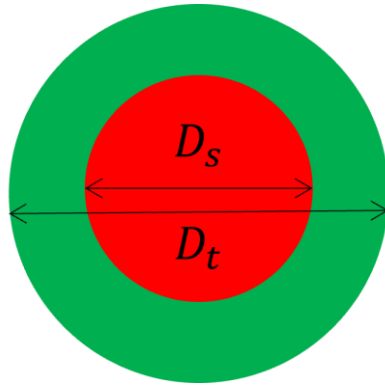


Figure 2.6. Intersection of the Target and Spot

As seen in the figure, spot area itself is the intersection area. Using the equation given below is used to calculate this area.

$$A_{intersection} = \pi D_s^2 / 4 \quad (27)$$

2.3.1.2 Rectangular Target

In the scenario where the transmitter is symmetric and the target is rectangular, four different situations were examined;

- If $(W/D_s)^2 + (H/D_s)^2 < 1$;

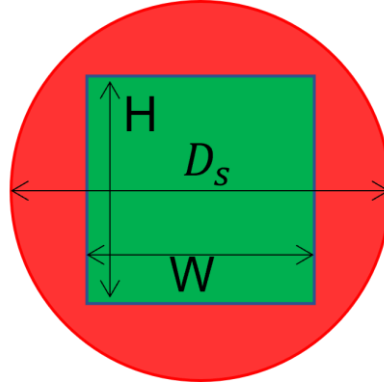


Figure 2.7. Intersection of the Target and Spot

In the figure, H is the height and W is the width of the target. The spot covers the target and the intersection area is target area itself given in the below equation

$$A_{intersection} = WH \quad (28)$$

- If $D_s \leq H$ and $D_s \leq W$;

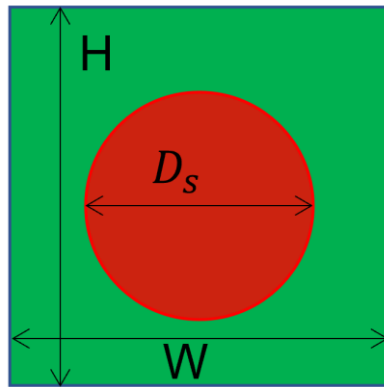


Figure 2.8. Intersection of the Target and Spot

As seen in the figure, target area covers the spot area. Intersection area is spot area and it is given

$$A_{intersection} = \pi D_s^2 / 4 \quad (29)$$

- If $D_s \leq H$ and $D_s \geq W$;

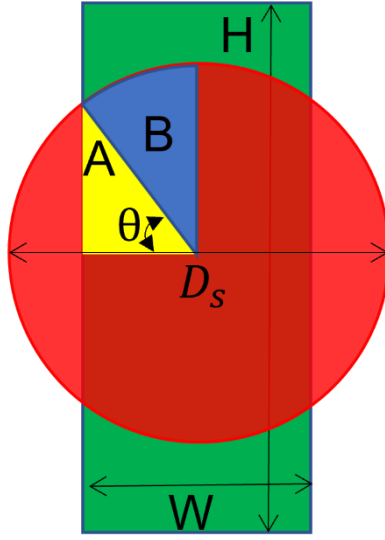


Figure 2.9. Intersection of the Target and Spot

$$A_{intersection} = D_s^2 / 4 (2(\pi/2 - \theta) + \sin(2\theta)) \quad (30)$$

$$\theta = \text{Acos}(W/D_s) \quad (31)$$

- If $D_s \geq H$ and $D_s \leq W$;

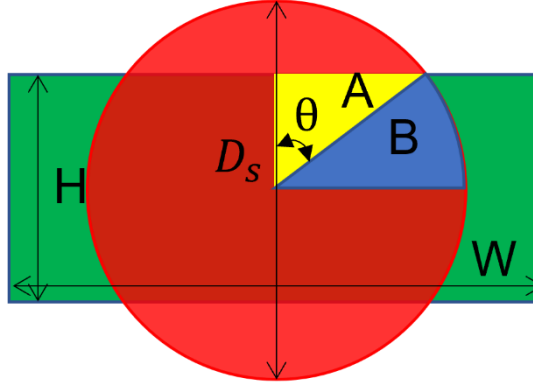


Figure 2.10. Intersection of the target and spot

$$A_{intersection} = \frac{D_s^2}{4} (2(\pi/2 - \theta) + \sin(2\theta)) \quad (32)$$

$$\theta = \arccos(H/D_s) \quad (33)$$

2.3.2 Intersection Areas in Asymmetric Case

In this section, spot is assumed to be elliptical. The cases where the target is circular and rectangular evaluated separately. In the following equations and figures, D_t is target diameter, D_{sx} is the horizontal and D_{sy} is the vertical spot diameter.

2.3.2.1 Circular Target

- If $D_{sx} \geq D_t$ and $D_{sy} \geq D_t$;

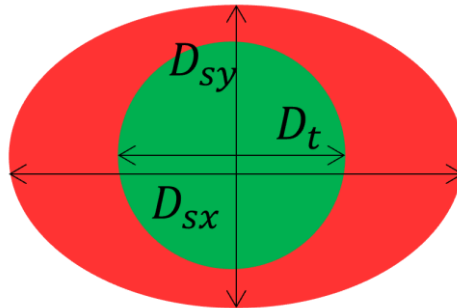


Figure 2.11. Intersection of the Target and Spot

$$A_{intersection} = \pi(D_t^2/4) \quad (34)$$

- If $D_{sx} \leq D_t$ and $D_{sy} < D_t$;

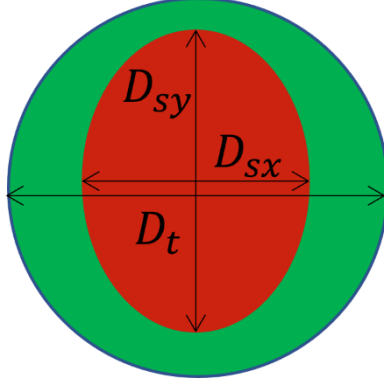


Figure 2.12. Intersection of the Target and Spot

$$A_{intersection} = \pi(D_{sx}D_{sy}/4) \quad (35)$$

- If $D_{sx} \leq D_t$ and $D_t \leq D_{sy}$;

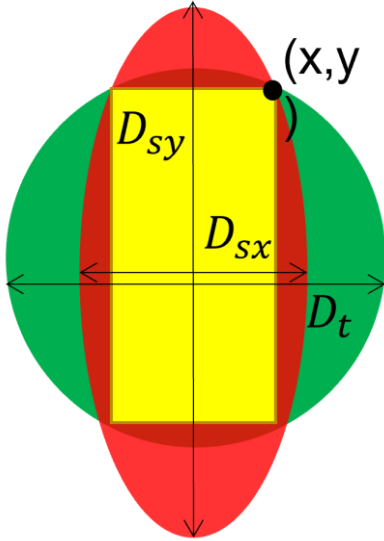


Figure 2.13. Intersection of the Target and Spot

$$A_{intersection} = D_{sx}D_{sy} \sqrt{(D_{sy}^2 - D_t^2)} \left(\sqrt{(D_t^2 - D_{sx}^2)} / \sqrt{(D_{sy}^2 - D_{sx}^2)} \right) \quad (36)$$

- If $D_{sy} \leq D_t$ and $D_t \leq D_{sx}$;

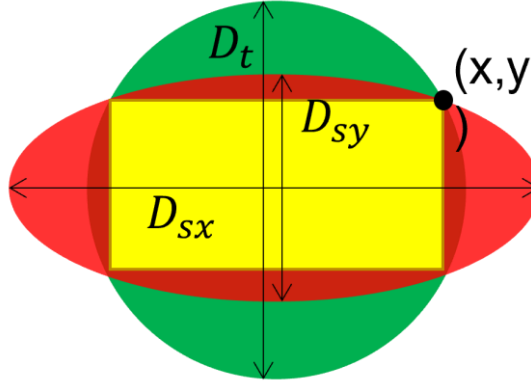


Figure 2.14. Intersection of the Target and Spot

$$A_{intersection} = D_{sx} D_{sy} \sqrt{(D_{sx}^2 - D_t^2)(\sqrt{(D_t^2 - D_{sy}^2)})} / \sqrt{(D_{sx}^2 - D_{sy}^2)} \quad (37)$$

2.3.2.2 Rectangular Target

- If $W/D_{sx}^2 + H/D_{sy}^2 < 1$;

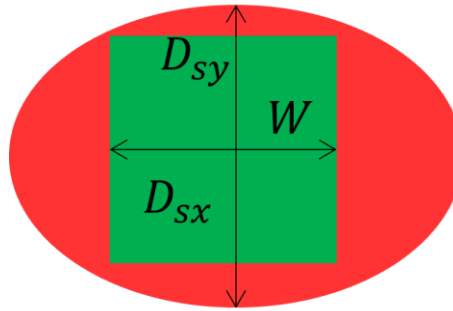


Figure 2.15. Intersection of the Target and Spot

$$A_{intersection} = WH \quad (38)$$

- If $D_{sy} < H$ and $D_{sx} < W$;

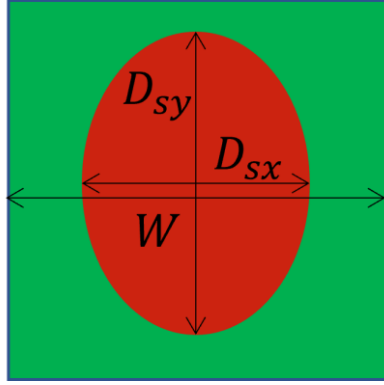


Figure 2.16. Intersection of the Target and Spot

$$A_{intersection} = \pi(D_{sx}D_{sy}/4) \quad (39)$$

- If $D_{sy} > H$ and $D_{sx} < W$;

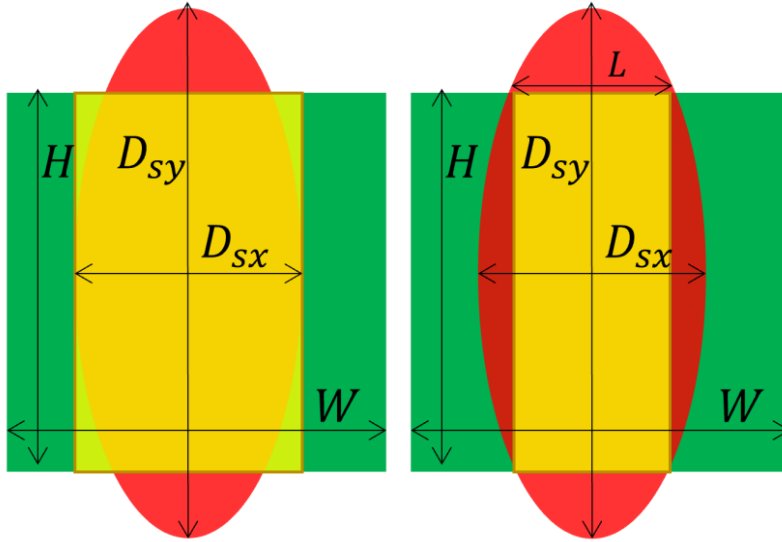


Figure 2.17. Intersection of the Target and Spot

$$L = D_{sx} \sqrt{1 - (H/D_{sy})^2}$$

$$A_{intersection} = (HD_{sx}) + (HD_{sx}) \sqrt{(1 - H^2/D_{sy}^2)} / 2 \quad (40)$$

- If $D_{sx} > W$ and $D_{sy} < H$;

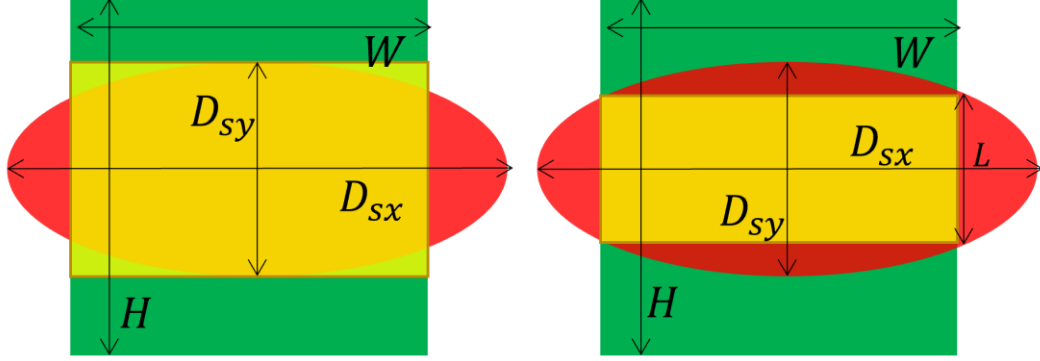


Figure 2.18. Intersection of the Target and Spot

$$L = D_{sy} \sqrt{1 - (W/D_{sx})^2}$$

$$A_{intersection} = (W * D_{sy}) + (W * D_{sy}) \sqrt{(1 - W^2/D_{sx}^2)} / 2 \quad (41)$$

Finally, optic power at the target can be found with the help of intersection areas of the spot and the target.

$$P_{target} = P_{transmitter} T_{a1} (A_{intersection}/A_{spot}) \quad (42)$$

2.3.3 Reflection Types

Laser light scatters and propagates according to the same set of principles that apply to radio frequency waves, namely, Maxwell's equations and boundary conditions [39]. Laser light, on the other hand, has such a short wavelength that even tiny particles and molecules can act as major scatterers. Target surfaces are often quite rough at laser wavelengths, and as a result, the diffuse reflection component

commonly dominates. In reality, in many situations, the laser cross section may lack a large specular component. However, strong specular reflections and retro-reflections from specific target surfaces have been seen on occasion. Diffuse and specular reflections are shown in Figure 2.19.

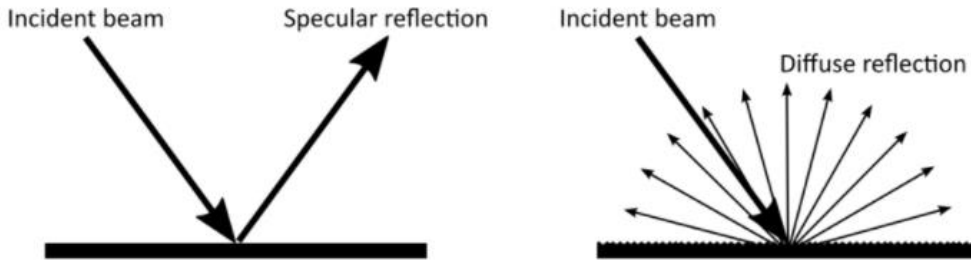


Figure 2.19. Reflection Types

In specular reflection, the beam is reflected from the target with its angle of incidence, while in diffuse reflection, reflection occurs in all directions independent of the incident angle. In addition, the total scattering pattern generated by a complex target illuminated by a laser beam is strongly influenced by the illumination incidence angle.

When looking at the diffuse reflection component, the highest amount of reflected energy is reflected at a 90° (normal) angle to the surface, and the energy goes down as a function of the cosine of the angle away from the surface normal.

A perfectly diffused surface distributes incident light evenly in all directions. The intensity (W/m^2) of diffusely reflected light for such a "perfect" surface is given by [22];

$$I_d = I_i k_d \cos \Theta \quad (43)$$

Where I_i is the intensity of the light source at the target, and Θ is the angle formed by the surface normal and line draw from the surface lit point to the light source.

The diffuse reflectivity, denoted by the constant k_d , is determined by the type of the material and the wavelength of the incoming light. Equation (44) may alternatively be represented as a vector:

$$I_d = I_i k_d (\hat{L} \hat{N}) \quad (44)$$

where \hat{L} and \hat{N} are the vectors shown in Figure 2.20.

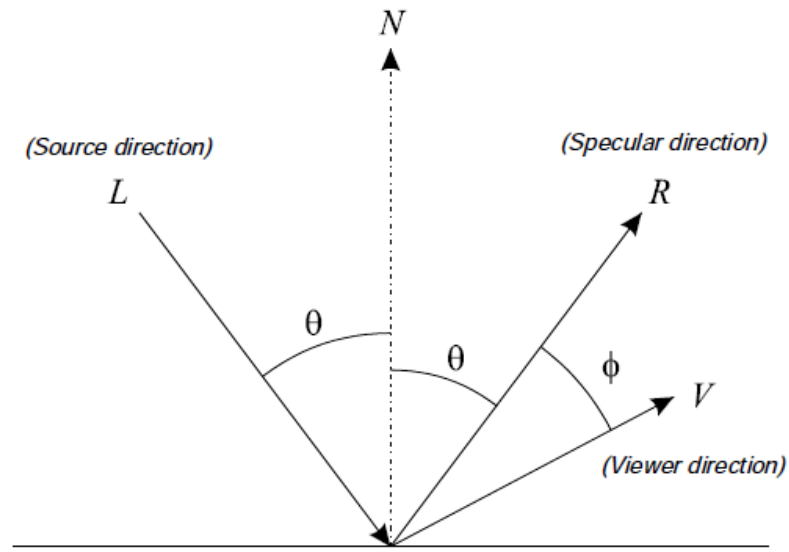


Figure 2.20. Reflection Geometry

Any reflection from a realistic surface should be regarded as the sum of a specular and diffuse component. The presence of these two components has been demonstrated empirically and is not a result of the model used. The surface roughness is an important surface characteristic to model. The incoming radiation is reflected in a single direction by a completely flat surface. A rough surface scatters incident radiation in all directions, although certain directions may have more reflected energy than others. This behavior is affected by the wavelength of the radiation; a smooth surface for some wavelengths may be rough for others.

Metal that has been oxidized or unpolished, for example, is smooth for radio waves but rough for NIR. Depending on whether or not they are polished, metals can be

diffuse or specular reflectors in the NIR. As a result, reflection is affected by both the material and its surface characteristics. A grazing angle of the incoming laser source is another element in reflection. The entity of the total reflected signal, as well as the two reflection components, may be determined using this method.

As a result, a "realistic" reflection model should include some combination of a perfect diffuse reflector and a perfect specular surface to represent the target surface. The Phong model [34] is one of the early and still popular models. This model may be used to match the findings of experimental bi-directional reflectivity measurements as well as for computer simulations. The bi-directional spectral reflectivity is calculated using the Phong model as follows:

$$\rho'_{\lambda} = k_{diff} + k_{spec} \cos\Phi^n \quad (45)$$

where, k_{diff} is the percentage of energy diffusely reflected and k_{spec} is the percentage specularly reflected. The model may be expressed in terms of the unit vectors related to the geometry of the point in the figure above.

$$I = I_i[k_d \cos(\theta) + k_s \cos\Phi^n] + A \quad (46)$$

$$I = I_i[k_d (L \cdot N) + k_s (R \cdot V)^n] + A \quad (47)$$

Where k_s is the specular reflection coefficient, n is the index that determines the dimensions of the specular highlight, and A is an extra component that accounts for sunlight reflection at the wavelength.

Figure 2.21 depicts the change in light intensity at a computed point P on a surface. A profile of the intensity variation is presented. The length of V from P to its junction with the profile determines the intensity at P. The diffuse term contributes to the semicircular section of the profile. For various values of the index n, the specular section of the profile is displayed.

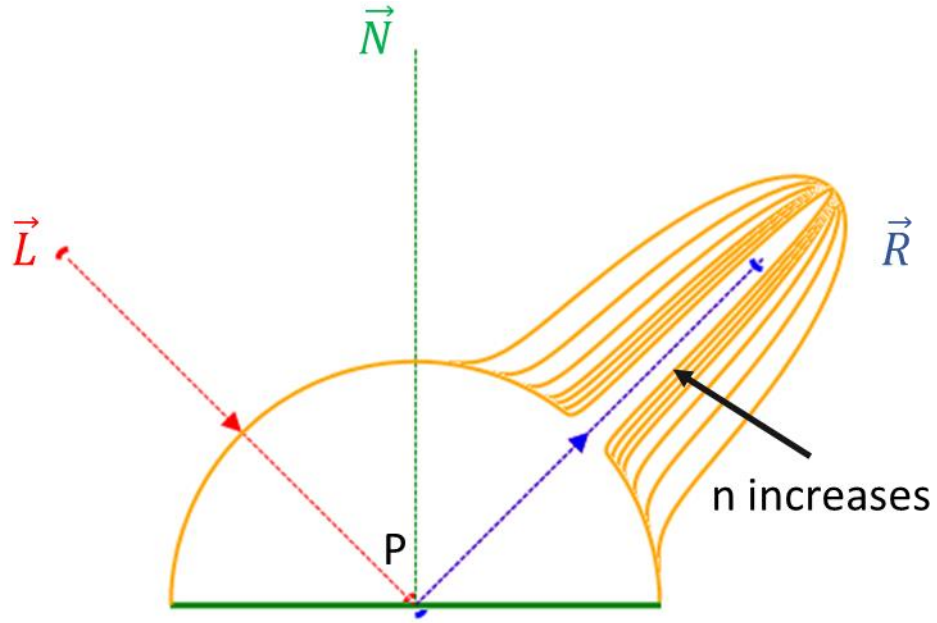


Figure 2.21. Phong Model

2.4 Detector Performance

The optical power collected in the receiver may be due to diffuse reflection only, specular reflection only, or the sum of both. This relationship is given in the equation below:

$$P_R = P_{R_S} + P_{R_D} \quad (48)$$

In the relation, P_R is the total power that reaches the receiver, P_{R_S} is the specular power and P_{R_D} is the diffuse power. In this section, the power reaching the receiver due to both types of reflection is examined separately.

First, the power reaching the receiver due to diffuse reflection was studied. As in the calculation of the power generated on the target, there must first be a power that reaches the distance where the receiver is located. This power can be calculated using equation below:

$$P_{R_D}' = P_t k_d T_{a2} \quad (49)$$

In the equation, P_{R_D}' is the power that reaches the distance where the receiver is, P_t is the power at the target, k_d is the diffuse reflection coefficient and finally T_{a2} is the atmospheric transmission between the target and the receiver.

After that, to find the power at the receiver, it is need to calculate the intersection area of the receiver and the spot due to diffuse reflection. The intersection area is calculated by using

$$A_{intersection} = \min (receiver\ area, diffuse\ spot\ area) \quad (50)$$

Finally, the optical power at the receiver due to diffuse reflection is

$$P_{R_D} = P_{R_D}' (A_{intersect} / A_{spot\ diffuse}) \quad (51)$$

2.4.1 Responsivity and Quantum Efficiency

The responsivity of a photodiode is a measure of its light sensitivity and is defined as the photocurrent to incoming light power ratio at a specific wavelength [41]:

$$R_\lambda = I_p / P \quad (52)$$

where, I_p is the photocurrent and P is the optical power that reaches the detector.

The portion of incoming photons that contribute to photocurrent is known as quantum efficiency. It is related to responsivity:

$$Q.E. = R_\lambda hc / \lambda q \quad (53)$$

Where h is the Plank constant in J.s, c is the speed of light in m/s, q is the electron charge in C and R_λ is the responsivity in A/W.

2.4.2 NEP

Photodetector sensitivity is a useful, though not essential, statistic for quantifying and comparing a photodetector's performance with that of other detectors. It is, nevertheless, difficult to define and verify. The NEP is a key metric for measuring the sensitivity of a photodetector or the power provided by a noise source [43]. The most commonly used definition for NEP is the following: The input signal power that results in a signal-to-noise ratio of 1 in a 1 Hz output bandwidth [35]. The NEP of a detector expresses the device's sensitivity and is indicated in Watts per square root of Hertz (W/Hz). The NEP essentially indicates the minimal detectable power per square root bandwidth of a particular detector; in other words, it is a measure of the weakest optical signal that can be detected. As a result, it is preferable to have as low a NEP value as feasible, because a low NEP value equates to a lower noise level and hence a more sensitive detector. Because the detector's responsivity is wavelength dependent, the Noise Equivalent Power is also wavelength dependent. The following formula may be used to compute the NEP:

$$NEP = I_{tn}/R_{\lambda} \quad (54)$$

In the equation, R_{λ} is the responsivity in A/W and I_{tn} is the total noise of the detector. NEP values can vary from $10^{11} \text{ W}/\sqrt{\text{Hz}}$ for large active area photodiodes down to $10^{-15} \text{ W}/\sqrt{\text{Hz}}$ for small active area [36].

2.5 Laser Reflection Simulator

In order to do both component selection and performance evaluation in laser systems, optical power calculation algorithm has been developed. The information from the three components (transmitter, target, and receiver), as well as the atmospheric conditions, must be taken into consideration when calculating the power coming out

of the transmitter and reaching the receiver. The software created based on this basic approach is given in the following figure.

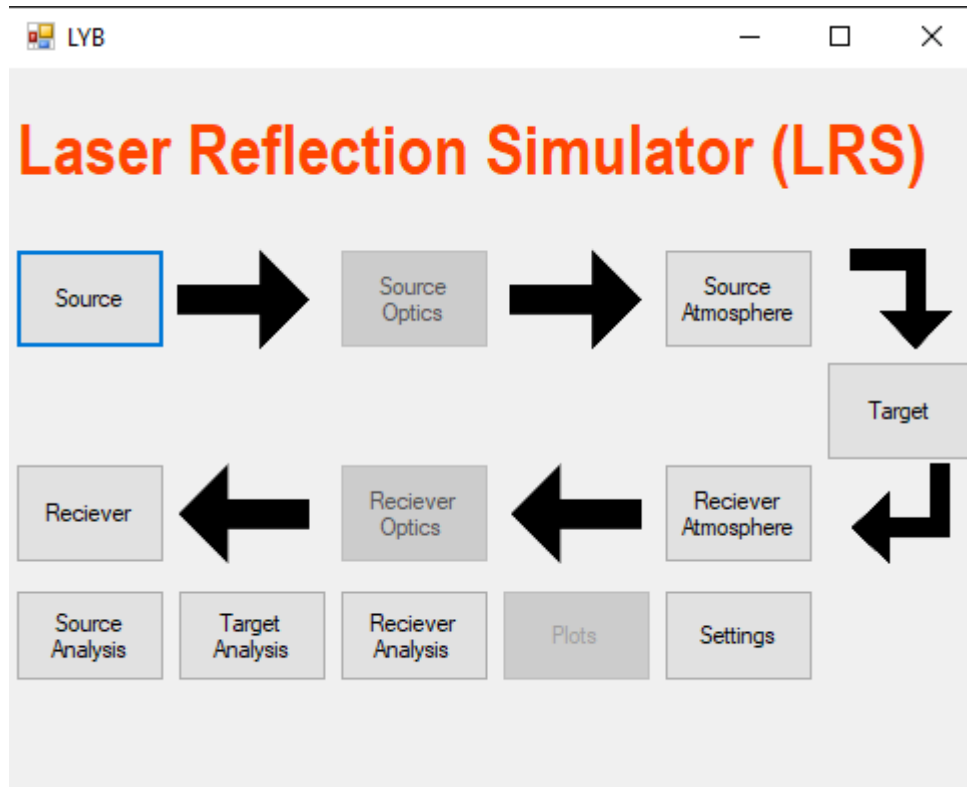


Figure 2.22. Main Form of The Software

As shown in the figure, the interface allows user to provide the design parameters in the order of path of the light: Source, Source Atmosphere, Target, Receiver Atmosphere, Receiver. After completing the input of the parameters, with the help of analysis forms, simulation results can be obtained. In this section, the steps of the design process with “Laser Reflection Simulator” will be demonstrated.

2.5.1 Input Forms

These forms provide the necessary interface for users to determine design parameters. Each form has its own library that consists of off the shelf component information. User may also define a custom component by providing information manually. In addition to this, each input parameter is supplemented with an

explanatory image to guide users. The designer may use the input forms in any order however there is a suggested order that is shown with arrows in Figure 2.21. Moreover, the designer may go back to previous forms to make revisions.

When the suggested order is followed, the design would start with the source form, Figure 2.23.

The 'Source' form is a window with a title bar containing a standard icon, a minus sign, a maximize button, and a close button. Below the title bar is a 'Source Name:' label followed by three buttons: 'New', 'Open', and 'Save'. There are two tabs: 'Pulsed' (selected) and 'Continuous Wave'. Below the tabs is a table with two rows: 'Peak Power' with value '1.20e02' and unit 'W', and 'Wavelength' with value '9.05e02' and unit 'μm'. Below this is another set of tabs: 'Symmetric Propagation' (selected) and 'Asymmetric Propagation'. Below these tabs is another table with four rows: 'Beam Divergence X' (90.00 e-01 mrad), 'Diameter X' (1.00e01 mm), 'Beam Divergence Y' (25.00 e00 mrad), and 'Diameter Y' (1.00e01 mm). At the bottom of the form is a diagram of a laser beam. The beam is represented by a red cone originating from a grey cylinder. The cone's edges are labeled with $\theta_x/2$ and the total angle is labeled θ_x . At the very bottom of the window are two buttons: 'Power Analysis' and 'Next'.

Figure 2.23. Source Form

As can be seen in the figure, the first part of the form allows user to interact with off the shelf component library. It is possible to save the custom source to the library to be used in later simulations. There are two source options with respect to wave types: pulsed and continuous. In the example, 905 nm pulsed laser source with 120 W power is designed. Laser propagation may be symmetric or asymmetric. In the

figure, it can be seen that asymmetric propagation is chosen and horizontal beam divergence is selected, thus the supplementary image of beam divergence is displayed on the bottom section of the form. By clicking the “next” button on this form or the source atmosphere button on the main form, “source atmosphere” can be reached, Figure 2.24.

Figure 2.24. Source Atmosphere Form

The top section of the form is similar in all input forms. In this form, the distance between the source and the target is inputted as “Range”. The angle between the normals of source and the target is inputted as “Angle”. Finally, the effect of the atmospheric transmittance is modelled with the “Transmittance” input. The user may

either input the transmittance value manually or use Modtran's atmosphere and aerosol model to be calculated automatically.

Most designs require the source and receiver to be positioned in a single unit. For these cases, coupling the position and/or atmosphere is provided. In the figure that is displayed in the bottom section of this form, source, target and receiver is represented with red, green and blue colors respectively. Whereas the “previous” button leads to source form, the “next” button leads to target form, Figure 2.25.

Target

Target Name:

New Open Save

Material

Material Selection: Kullanıcı Tanımlı

Diffuse Coefficient	3.00e-01
Specular Coefficient	7.00e-01

Spherical Rectangular

Width	1.00e01	m	▼
Height	2.00e01	m	▼
Area	2.00e02	m ²	▼

Diagram illustrating the target geometry and incident radiation angles θ_i .

Previous Target Analysis Next

Figure 2.25. Target Form

The reflective properties of various materials are provided within the software, yet diffuse and specular coefficients can be edited manually. Currently, the software allows spherical and rectangular target shapes. In the example demonstrated in the figure, a rectangular target with area 200 m² is defined that reflects specular dominantly. From this form, the user may directly reach “source atmosphere”, target analysis and receiver atmosphere, Figure 2.26.

Figure 2.26. Receiver Atmosphere Form

Similar to the source atmosphere, the distance between target and receiver, the angle between target and receiver normals are required. In the example demonstrated, due to the fact that the source and receiver atmospheres were coupled in the “source

atmosphere” form previously, there is no need to individually model the atmosphere affect.

The last of the input forms is for the receiver.

The screenshot shows a software window titled "Reciever". It has a "Reciever Name:" label and three buttons: "New", "Open", and "Save". Below these are three tabs: "Photodiode", "Camera", and "Powemeter", with "Photodiode" selected. The "Photodiode" tab contains a table of parameters:

Responsivity	5.80e-01	A/W	▼
Quantum Efficiency	75.73	%	▼
Noise Equivalent Power (NEP)	6.00e01	W/√Hz	▼
Detectivity	1.67e-02	√Hz/W	▼

Below the table are two tabs: "Spherical" and "Rectangular", with "Rectangular" selected. This section contains another table:

Diameter	4.50e01	mm	▼
Area	1.59e-03	m ²	▼

At the bottom of the form is a graph titled "Spectral Response". The y-axis is labeled "Responsivity (A/W)" and ranges from 0 to 0.7. The x-axis is labeled "Wavelength (nm)" and ranges from 300 to 1100. A red curve shows the spectral response, starting at approximately 0.1 A/W at 300 nm, rising to a peak of about 0.6 A/W at 950 nm, and then falling to about 0.1 A/W at 1100 nm.

At the very bottom of the window are two buttons: "Previous" and "Reciever Analysis".

Figure 2.27. Receiver Form

Receiver is categorized into three types: photodiode, camera and power meter. For the extend of this thesis, only photodiodes are examined; therefore, the software currently only works with the photodiode option. In order to model a photodiode, responsivity or quantum efficiency and NEP or detectivity input must be provided. Additionally, the sensor geometry is inputted.

2.5.2 Analysis Forms

There are three analysis forms: source, target and receiver. Source analysis is used to determine the peak power of cont. Wave laser. For the extend of this thesis, this analysis is excluded on account of the fact that only pulsed lasers are considered in the design.

The second analysis form is for the target, Figure 2.28.

Spot Analysis Results		
Laser Spot Width	9.01e00	m
Laser Spot Height	2.50e01	m
Laser Spot Area	1.77e02	m ²
Target Front Surface Area	2.00e02	m ²
Intersection (Reflection) Area	1.44e02	m ²

Power Analysis Results		
Power at Distance	6.30e01	W
Power at the Target	5.13e01	W
Specular Reflected Power	3.59e01	W
Diffuse Reflected Power	1.54e01	W

Figure 2.28. Target Analysis Form

The results for the target analysis is separated into two sections. In the first section, the geometrical analysis is done to determine laser spot size, target and intersection area as explained in section 2.3. As can be seen on the right of the numerical outputs,

the results are also visualized for the ease of interpretation. The second half of the form, the results of the power analysis can be observed. On the picture box next to the power analysis, the reflection model is drawn as explained in section 2.2.1.

Finally, the most important results are placed in the receiver analysis form, Figure 2.29.

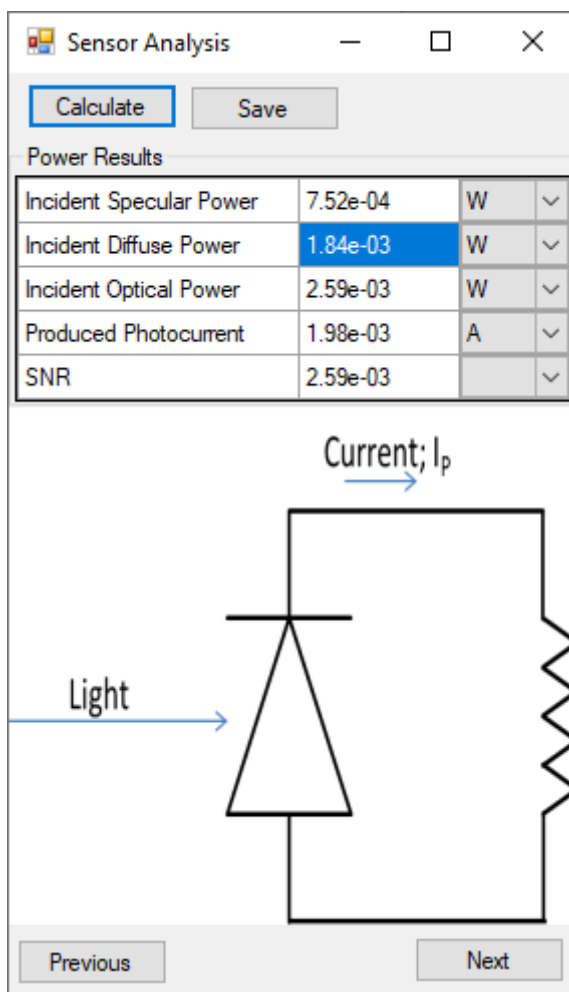


Figure 2.29. Sensor Analysis Form

The specular and diffuse optical powers reaching the receiver is calculated individually, which is combined to determine photocurrent. With the help of the detectivity, SNR is also calculated. All these results that allows us to evaluate the performance of the design are provided in this form.

Thanks to this software, the performance of each combination of possible receivers and transmitters that will be determined by market research is easily and quickly determined.

By completing the essential market research for the project, it has been determined that three distinct transmitters may be suitable. These components' electronic characteristics and requirements have been used in electronic and optical design research.

After determining the possible transmitters and receivers, a sample scenario was calculated by assuming an extended target with a reflection coefficient of 0.1 at a distance of 40 m in order to provide input to the optical design. The characteristics of the transmitters used are given in Table 2.5 and the characteristics of the receivers are given in Table 2.6.

Table 2.5 Transmitters Properties

	Peak Power (W)	Beam Div. (°)	Aperture (μm)
V1	75	9X25	200X10
V2	30	10X25	75X15
V3	80	12X20	235X10

Table 2.6 Receivers Properties

	Type	Active Area (mm ²)	Responsivity (A/W)
A1	Pin Diode	42	0.60
A2	Pin Diode	13	0.56
A3	Pin Diode	5	0.62
A4	APD	19.6	0.20
A5	Pin Diode	5	0.58

Optical power reaching the receiver was calculated by using the algorithm with different beam divergence values for each transmitter-receiver pair. By using these optical power results and the sensitivity values of the receivers, the photocurrent generated in the receivers was obtained. The results generated for the A1 numbered Receiver and V1 numbered Transmitter pair are given in Table 2.7.

Table 2.7 A1 – V1 Pair Performance

Beam Divergence	Power at Receiver (W)	Photo Current (A)
9x25 (°)	1.18E-06	7.08E-07
9x25 (mrad)	2.79E-04	1.67E-04
15x15 (mrad)	2.79E-04	1.67E-04
10x10 (mrad)	6.27E-04	3.76E-04
9x9 (mrad)	7.74E-04	4.64E-04
8x8 (mrad)	9.79E-04	5.87E-04
7x7 (mrad)	1.28E-03	7.68E-04
6x6 (mrad)	1.74E-03	1.04E-03
5x5 (mrad)	2.51E-03	1.51E-03
4x4 mrad	3.91E-03	2.35E-03
3x3 (mrad)	6.96E-03	4.18E-03
2x2 (mrad)	1.56E-02	9.36E-03
1x1 (mrad)	6.25E-02	3.75E-02

The results obtained from all receiver – transmitter pairs are given in Figure 2.30.

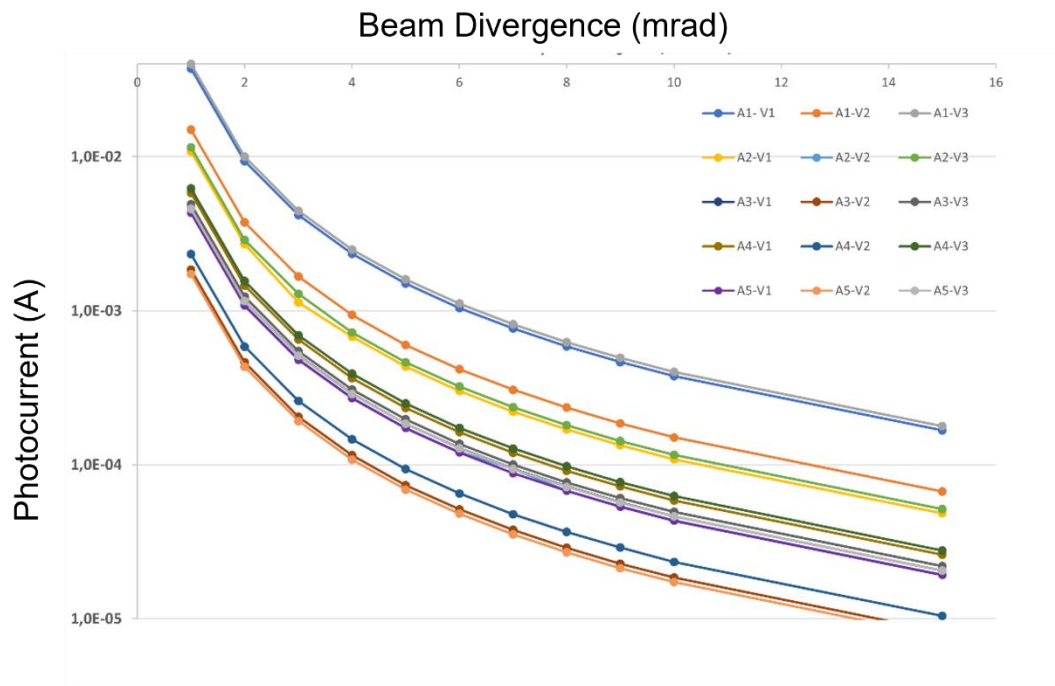


Figure 2.30. Photocurrent – Beam Divergence Graph

When the graph is examined, it is seen that the amount of light reaching the receiver and therefore the current on the sensor increases with the decrease of the beam divergence value.

CHAPTER 3

OPTICAL SYSTEM DESIGN

In LIDAR systems, the laser must be guided at the target with the least amount of energy loss possible. Likewise, the light reflected from the target must be gathered by the receiver. In this section, it is aimed to make a transmitter - receiver design in which the laser will have the smallest divergence angle and all the rays returning from the target will be collected in the receiver.

Depending on the requirements determined from laser beam geometry, detector size, and so on, special optical design is necessary. Even though off – the – shelf optical components may be less expensive, custom design optical components are frequently employed to fulfil system requirements. Commercial optical system design software was used to develop and analyze optical components. This software can execute ray tracing in two separate modes: sequential and non-sequential. The user defines the ray tracing sequence in sequential mode by defining the order of surfaces. The surface ordering has no effect on ray tracing in non-sequential mode. In the Optical design software's sequential mode, it is not feasible to replicate a direct laser diode source due to the astigmatic light characteristic. Therefore, transmitter design was done in non sequential mode. On the other hand, receiver design was made using sequential mode.

3.1 Transmitter Optical Design

The laser beam coming out of the laser diode is highly divergent. The beam divergences of laser that is used in this study are 10° and 25° respectively horizontal and vertical. The NSC (Non-Sequential) simulation of this laser at fast and slow axis is given in the Figure 3.1 and Figure 3.2 respectively.

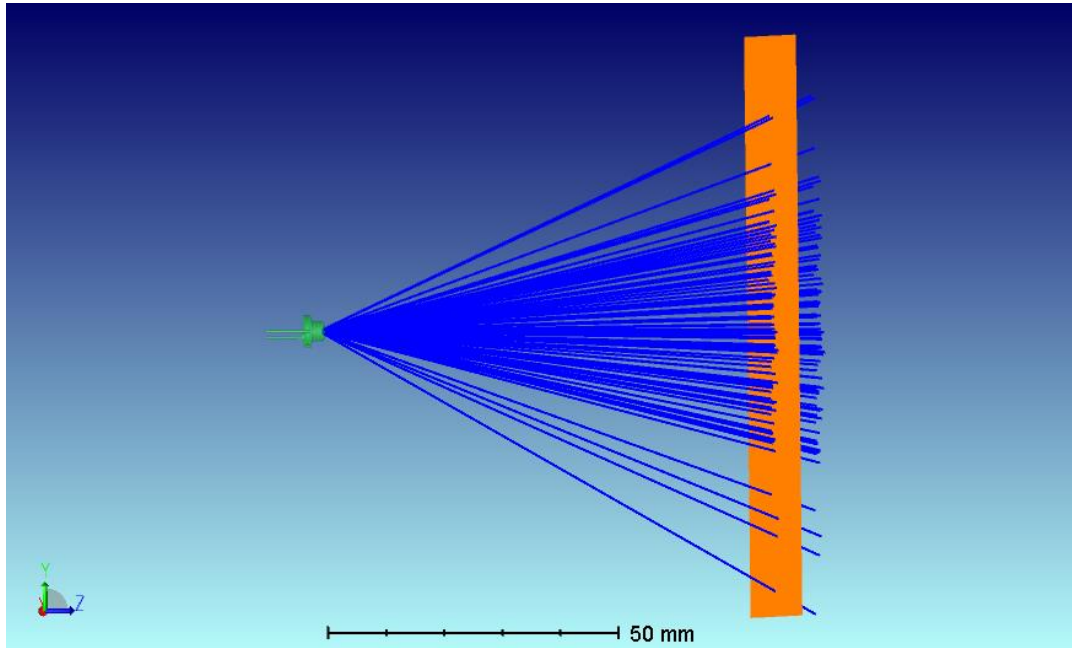


Figure 3.1. NSC Fast Axis Simulation

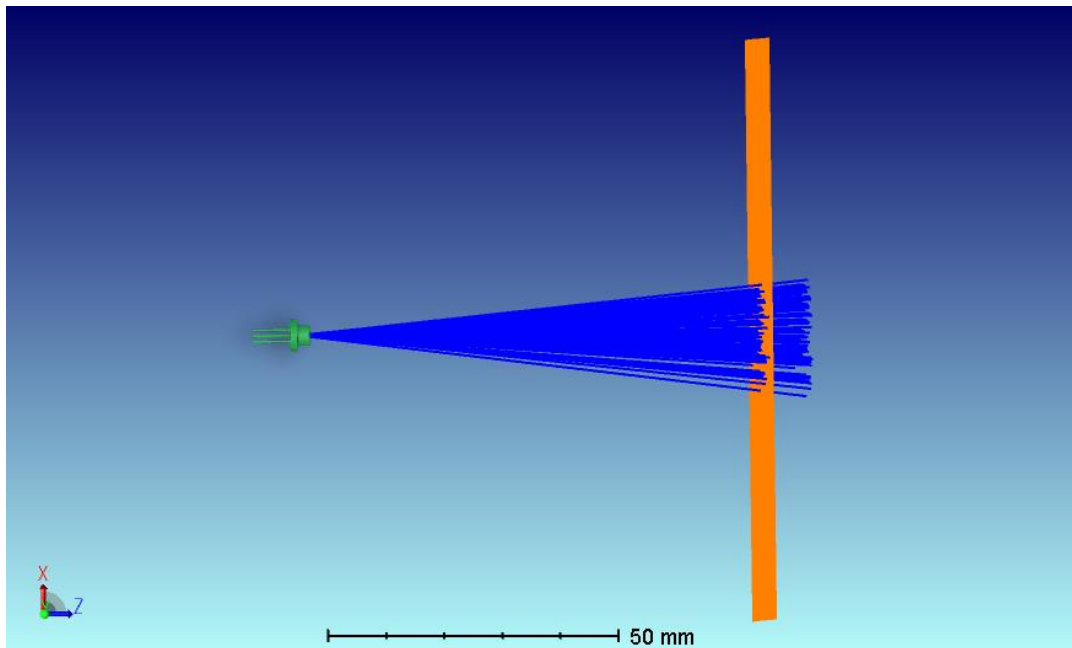


Figure 3.2. NSC Slow Axis Simulation

The shape of the spot that forms on the detector is given in the Figure 3.3.

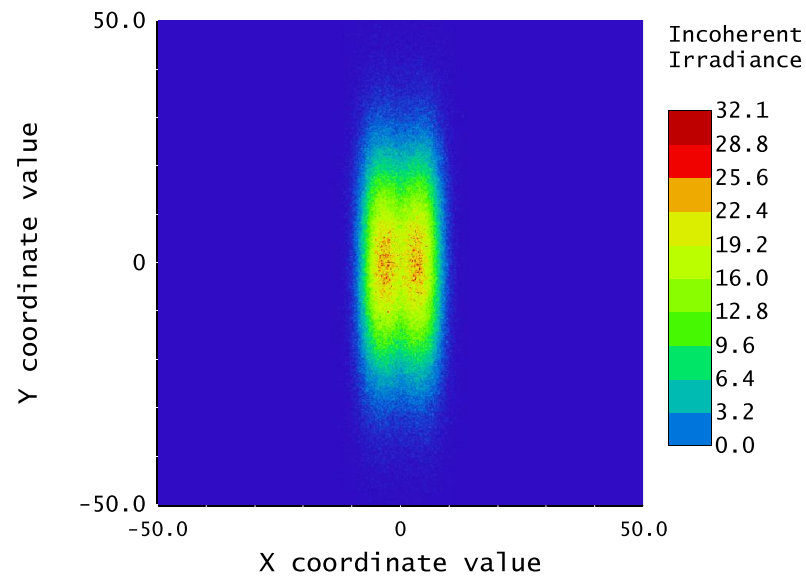


Figure 3.3. Detector View of Laser Diode

As can be seen in the figure, these light rays must be collimated at fast and slow axes. Fast axis represents the large beam divergence and the slow axis represents the small beam divergence when compared to another axis [37].

In the literature, there are two main methods to collimating laser diode, The first method is using a single aspheric lens. Aspheric lenses can collimate diode in only one axis as shown in the Figure 3.4.

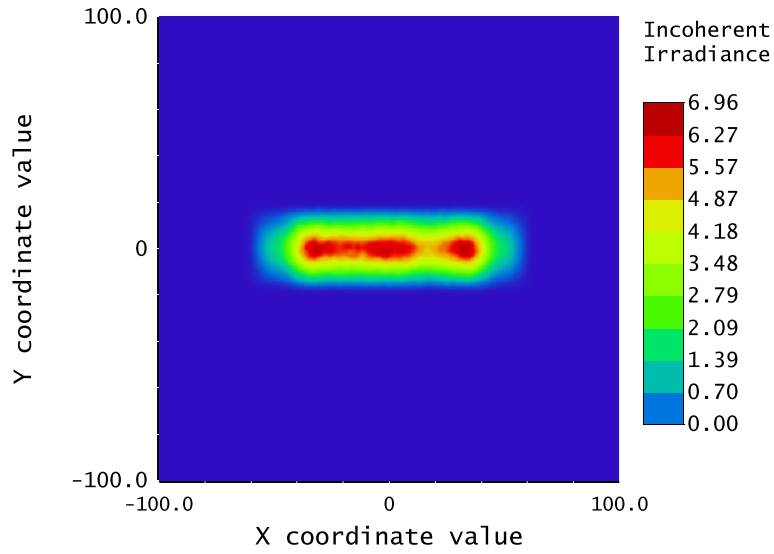


Figure 3.4. Detector View of Aspheric Design

The fact that aspheric lenses are axisymmetric causes this result. In addition to this, aspherical lenses are expensive and hard to manufacture. It is difficult to measure the aspheric parameters after manufacturing. Thus, this method is not preferred.

The second widely used method is cylindrical lenses [38]. This method is usually used to turn an elliptical spot into a circular one. In this design, there are two cylindrical lenses. One of these lenses acts on the fast axis, while the other acts on the slow axis as shown in the Figure 3.5.

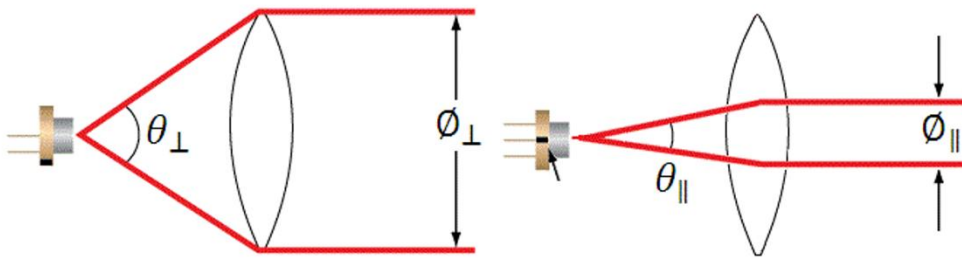


Figure 3.5. Fast (Left) and Slow (Right) Axis of Laser Diode

In the figure, Θ represent the beam divergence of laser and \emptyset represents the aperture of the lens. The equation used to find the focal length of cylindrical lens is given equation (55).

$$f = \frac{\frac{\emptyset_{\perp}}{2}}{\tan(\frac{\theta_{\perp}}{2})} \quad (55)$$

The equation given above is used to find the focal length of the lens positioned close to the laser (acting on the fast axis). It has been mentioned before that the fast axis angle of the laser is 25° . Considering a lens with an optical aperture of 4 mm, the focal length is found to be 8.12 mm when the above formula is used. After the theoretical focal lengths of the lenses were found, the system was optimized, and the best Z positions of these lenses were found.

The effect of the first lens is shown in the Figure 3.6.

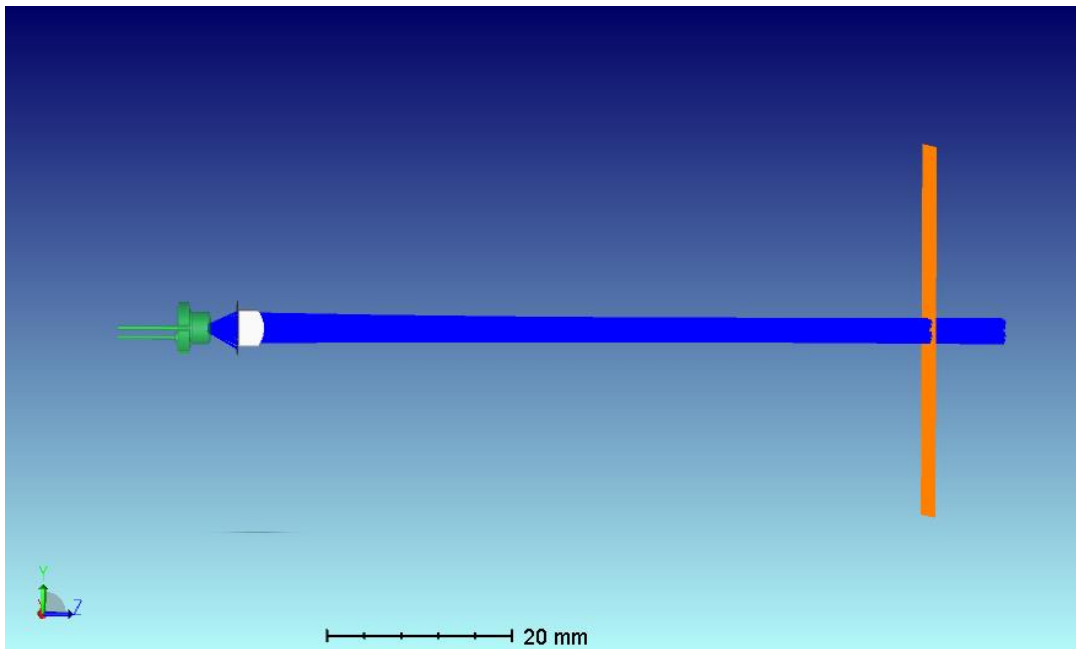


Figure 3.6. Effect of the First Lens on Fast Axis

As can be seen from the figure, this lens affects the fast axis. This lens does not affect the slow axis. the slow axis view is given in the Figure 3.7.

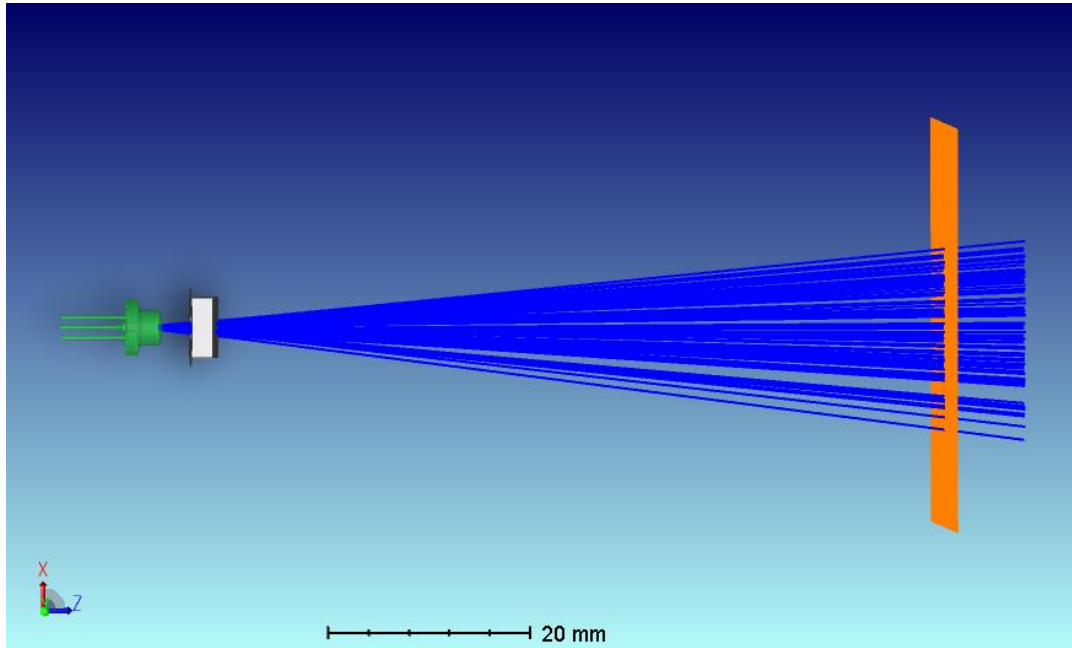


Figure 3.7. Effect of the First Lens on Slow Axis

The detector viewer after the first lens is added to design is given in the Figure 3.8.

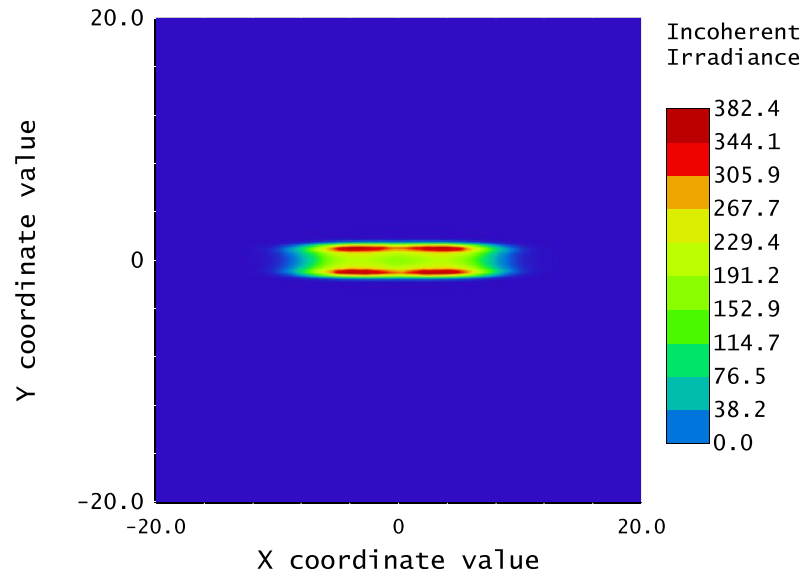


Figure 3.8. Detector View

As seen in the figure, the spot in the direction of the fast axis has reduced, as predicted.

After determining the best location of the first lens in the Z direction (optical axis), the second cylindrical lens is included in the system. Fast axis and slow axis view of the design is shown in the Figure 3.9 and Figure 3.10 respectively.

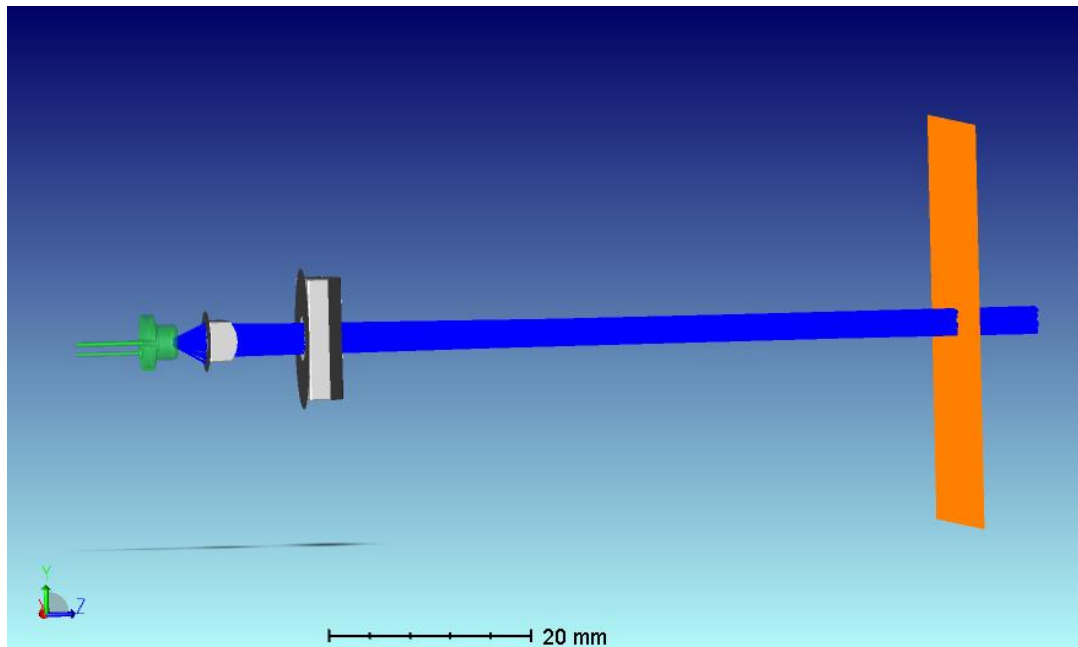


Figure 3.9. Fast Axis View of the Design

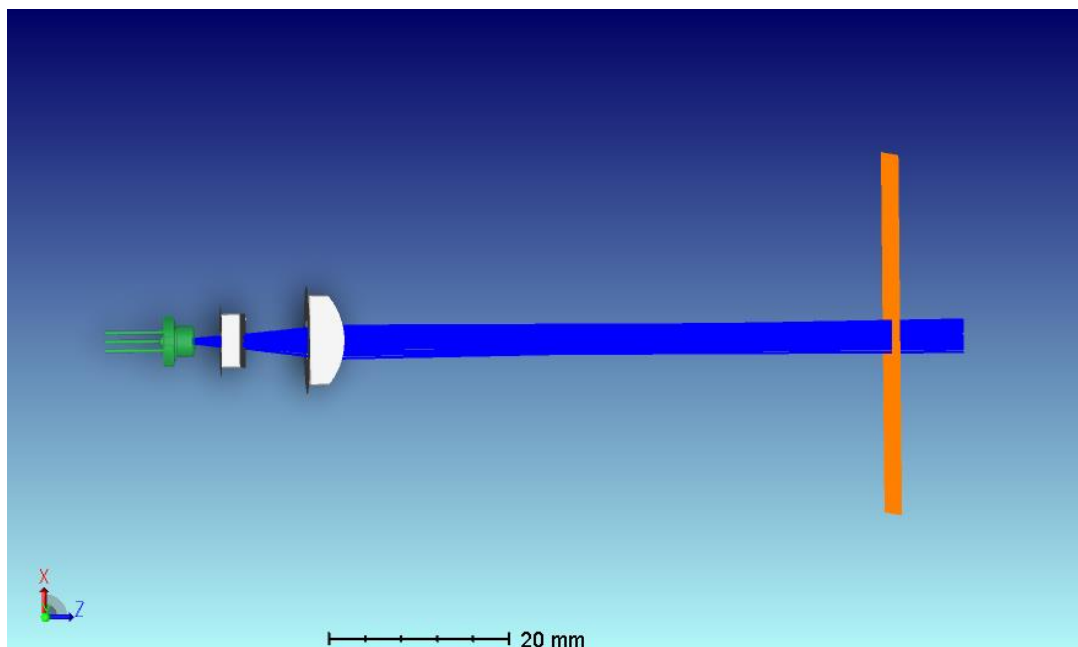


Figure 3.10. Slow Axis View of the Design

The image of the spot formed on the detector is given by Figure 3.11.

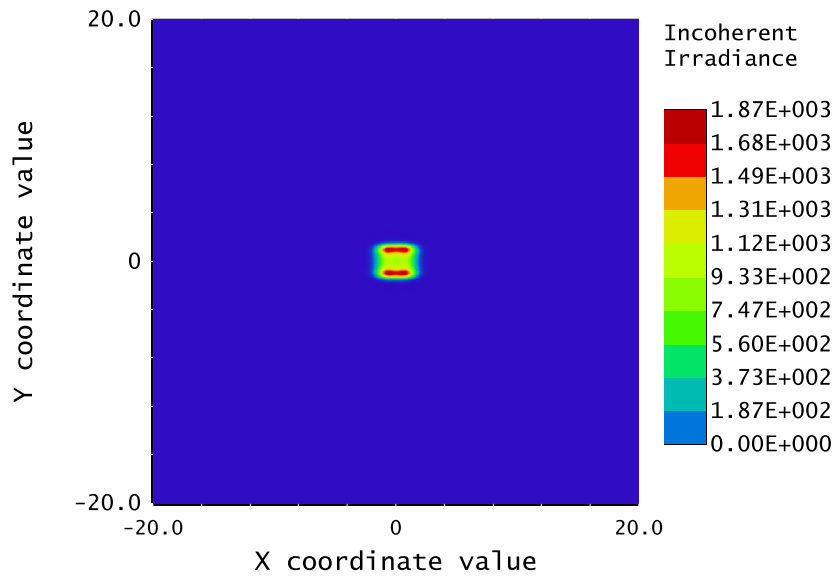


Figure 3.11. Detector View of the Design

Because of the astigmatic nature of the laser diode, generating a circular beam by reducing the divergence angles of the two axes may not be achievable.

The spot sizes and beam divergence values measured at different distances are given in the Table 3.1.

Table 3.1 Spot Size and Beam Divergence of the Design

Distance (mm)	Spot Size (mm)		Divergence (degree)		Divergence (mrad)	
	Horizontal	Vertical	Horizontal	Vertical	Horizontal	Vertical
1000	14.87	10.22				
2000	29.34	18.05	0.8	0.4	14.5	7.8
5000	72.17	42.42	0.8	0.5	14.3	8.1
10000	142.8	84.04	0.8	0.5	14.1	8.3

After the completion of the transmitter design, the analysis was performed. In these analyses, the effects of the optical parameters used in the transmitter design on the

beam divergence and beam power (the light that can be delivered to the target) were examined. The analyzes are given below, respectively;

- The effect of the position of the first lens on the Z axis on the beam divergence on the Y axis,

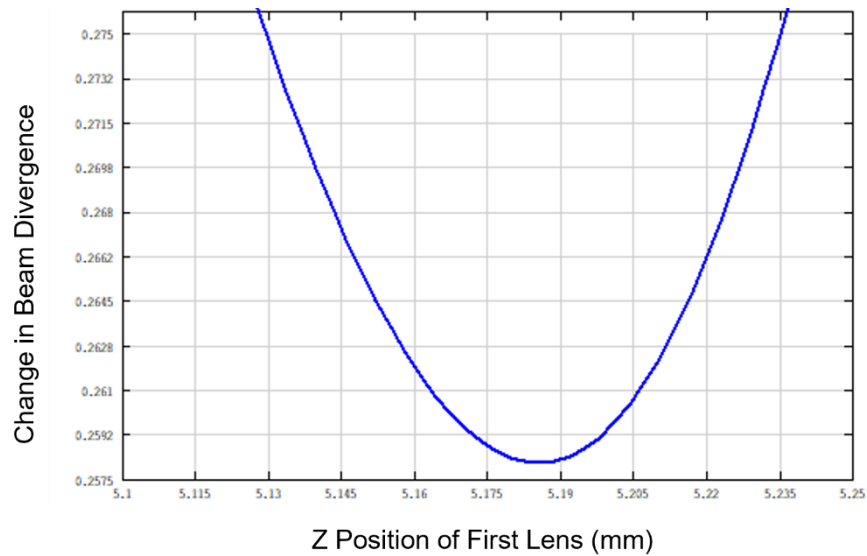


Figure 3.12. Z Position of First Lens – Beam Divergence Graph

- The effect of the position of the second lens on the Z axis on the beam divergence on the X axis,

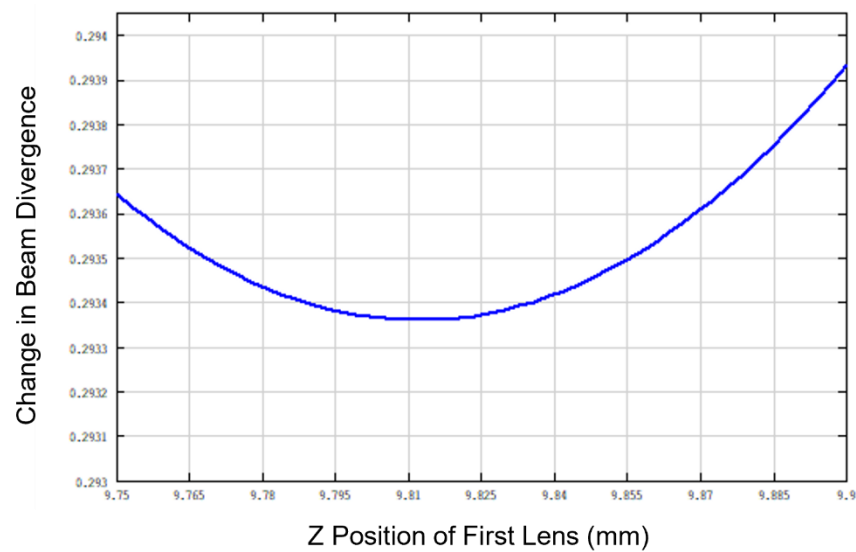


Figure 3.13. Z Position of Second Lens – Beam Divergence Graph

- The effect of the aperture of the first lens on the beam power,

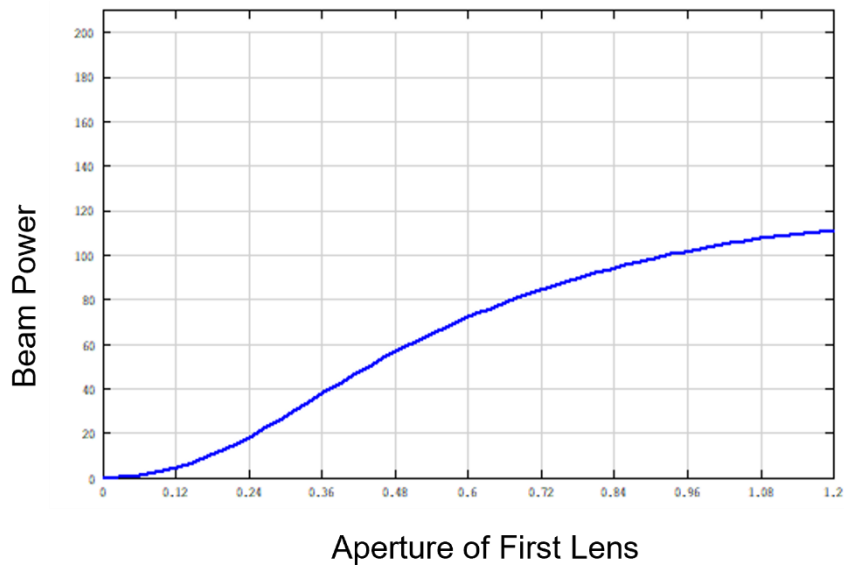


Figure 3.14. First Lens Aperture - Beam Power Graph

- The effect of the aperture of the second lens on the beam power,

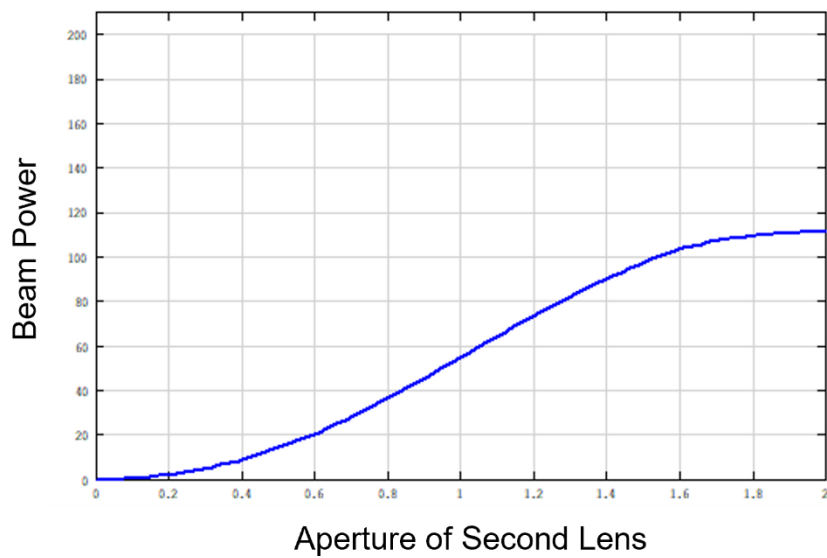


Figure 3.15. First Lens Aperture - Beam Power Graph

The analyzes carried out helped to find the manufacturing and integration tolerances of the lenses used, as well as to find the smallest beam divergence values that can be obtained with the current design.

3.2 Receiver Optical Design

The detector size is a critical parameter for the optical design of the receiver. In this study, APD with a diameter of 500 microns was used. Considering an optical system with a receiver and transmitter, the field of view of the receiver should be at least up to the transmitter beam divergence. At this point, considering that there is a moving part to scan, the need for the receiver's field of view to be between two and five times the beam divergence of the transmitter has been evaluated. Aspheric condenser lens was used in the receiver optical design, Figure 3.16.

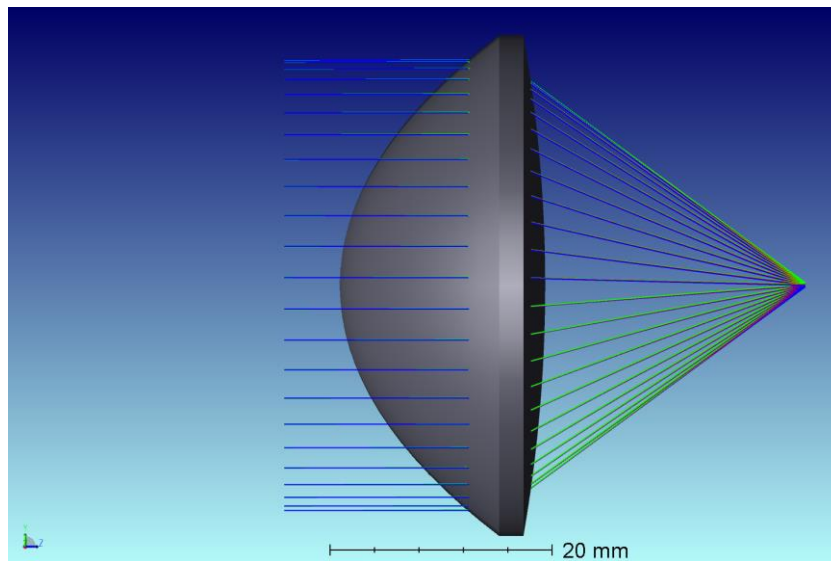


Figure 3.16. Receiver Optical Design

The most important tool for evaluating receiver design is the spot diagram. Spot Diagram of the receiver is given in the Figure 3.7.

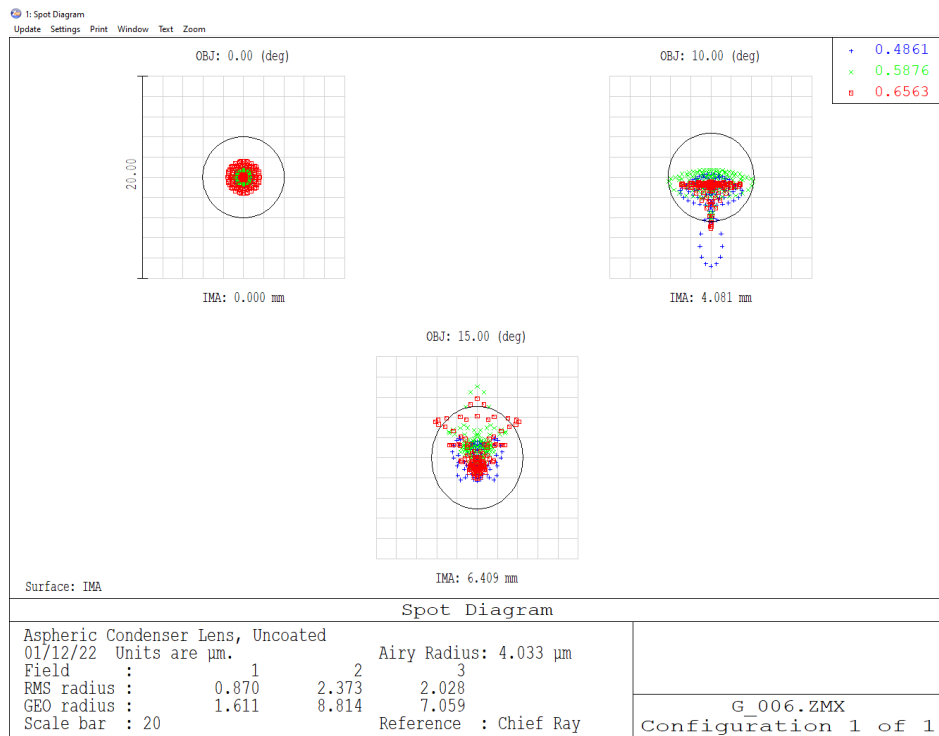


Figure 3.17. Spot Diagram of the Receiver

As mentioned in the 1.3.2, the RMS radius is important to understand whether the system is focused or not [48]. As shown in the figure, RMS radius is smaller than the airy radius, so the system is well focused.

Another important issue is the distance and the angle between transmitter and the receiver. The transmitter and the receiver are located as close as the mechanical structure allows. It has been evaluated that the optical axes of the transmitter and the receiver should be positioned parallel to each other due to the long ($>10\text{m}$) measurement distance and close positioning.

The designed model of the receiver is given in Figure 3.18.

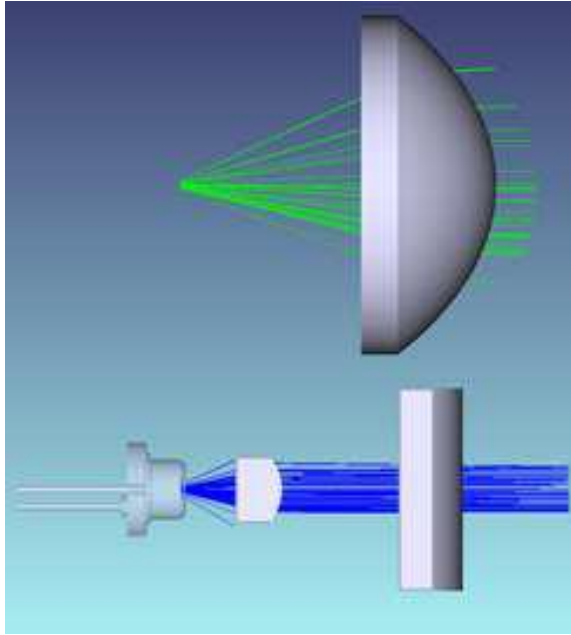


Figure 3.18. Transmitter - Receiver Design

After the completion of the Receiver and Transmitter optical designs, mirror dimensions and placement studies have been started for the scanning system. The scanning system is a 45° angle placed on the transceiver it is based on 360° rotation of the mirror. The scanning model is given in the Figure 3.19.

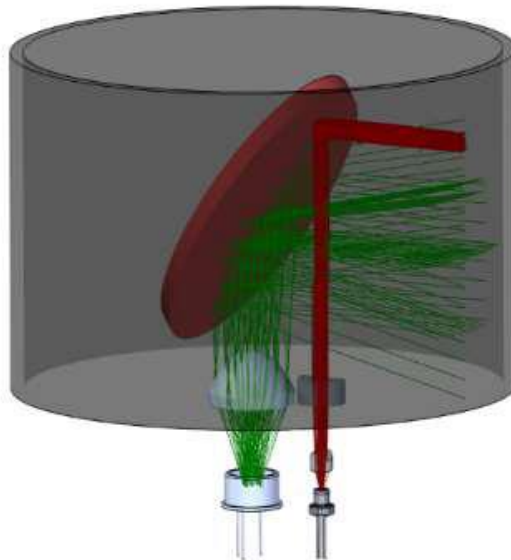


Figure 3.19. Scanning System

The window seen in the figure that separates the scanning mechanism from the external environment also acts as a filter. The transmission graph of this window is given in the Figure 3.20.

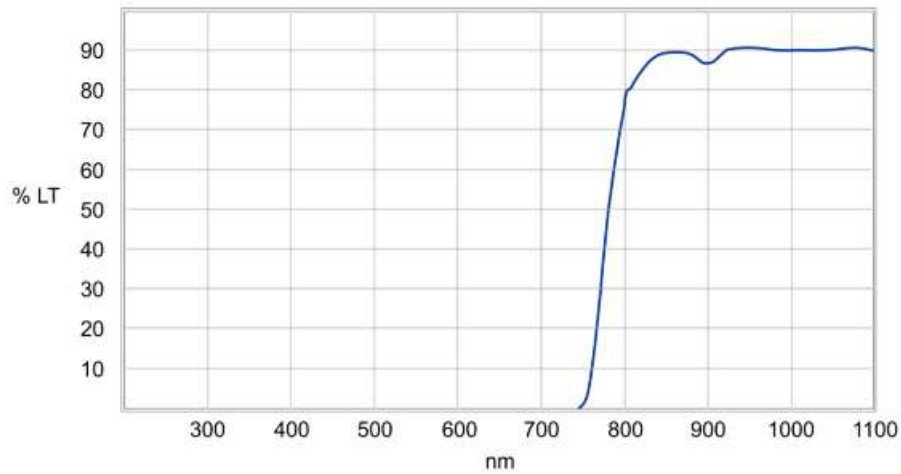


Figure 3.20. Transmission Graph of the Window

CHAPTER 4

OTHER SYSTEM COMPONENTS

In this section, electronic, mechanical and software design studies are explained. These studies were made by my valuable colleagues who are experts in their fields in Rekrom Optoelectronics.

4.1 Electronic Design

For the laser source to be driven at different parameters and powers, a special driver circuit design has been made for the system, Figure 4.1. Pulsed lasers have repetition rate restrictions. Due to this limitation, the pulse repetition rate should be reduced as the width of the barbe signal is increased. The transmitter board can drive a laser with a wavelength of 905 nm with pulse signals up to 20 kHz.

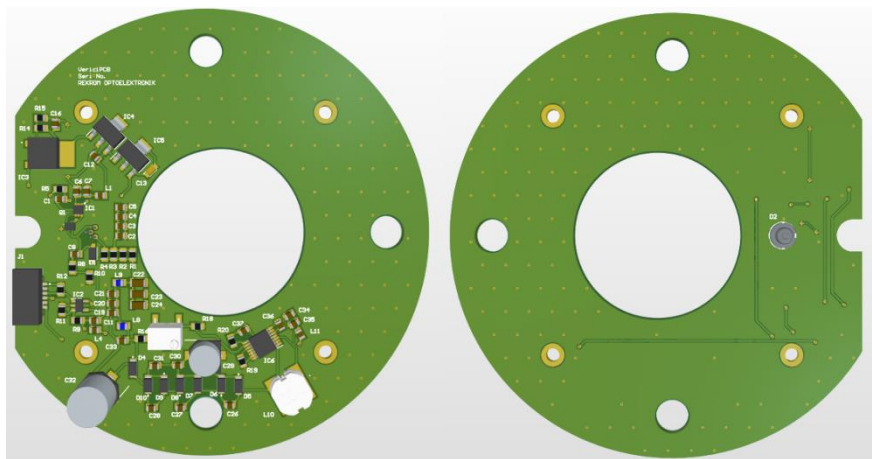


Figure 4.1. Transmitter PCB

To read the signal formed on the light sensing unit (photodetector) in the system, a special circuit design has been made that includes various amplifier and rectifier electronic components, as well as a microcontroller and counter unit, Figure 4.2. A simple component with an operating repetition rate of 100 MHz is used as a

microcontroller. The microcontroller manages the communication protocols as well as the control of the counter unit.

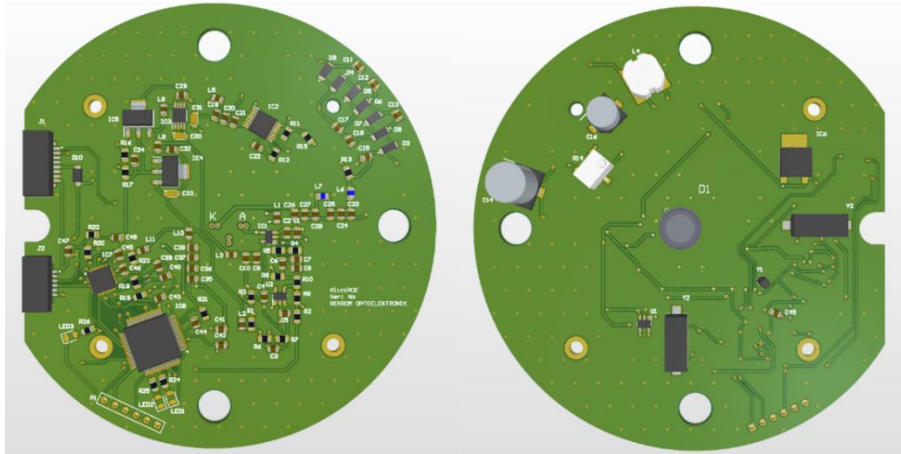


Figure 4.2. Receiver PCB

A counter circuit has been pre-designed in LIDAR, which can calculate time of flight of the laser, suitable for the transmitter and receiver circuits. In this design, a customized Time-to-Digital Converter (TDC) is used that can calculate the time difference between the two outgoing and incoming signals in picosecond resolution and transmit it to the microcontroller as a digital number. The first step in the process is for the TDC to ignite the laser source and thus start the counter. After the echo signal reflected from the target falls on the photodetector, it is amplified and converted into a digital signal with the comparator. The counting process ends with the digital signal being sent to the TDC and the counter is stopped.

In order to transfer the data produced by LIDAR to the computer environment, the necessary communication circuit has been pre-designed. RS485 is used as the communication protocol. As of now, in case of real-time communication and data transfer, the system can operate at 10 kHz. At this point, it is seen that the component that limits the speed is the low-cost microcontroller unit.

4.2 Mechanical Design

After the completion of the optical design studies, the design of the optomechanical structure was started in order to integrate the optics and electro-optical components. Optomechanical design started with the transfer of the optical model obtained as a result of the optical design studies to the mechanical design program. Considering the scope of the project, time, and budget constraints, it was decided to make the optomechanical production with a three-dimensional printer.

Apart from optical components, the placement of electronic circuit boards and the need for a shell to protect them against external factors have also shaped the optomechanical design. First of all, a suitable integration interface has been designed on optomechanics for the integration of electronic cards. Then, the necessary interfaces are designed so that the receiver - transmitter can be integrated into the shell. After the completion of the design, the production of the parts was carried out and the integrations were made. The resulting optomechanical structure is given in the Figure 4.3.

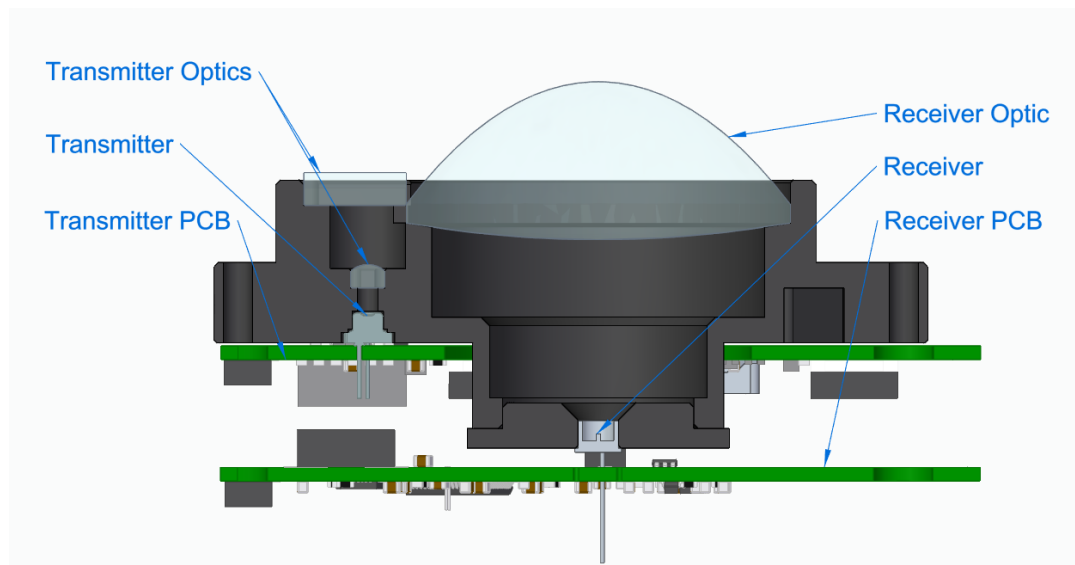


Figure 4.3. Optomechanical Design

4.3 Software Design

A user interface is built to visualize LIDAR outputs. This interface is written in C++ using open source libraries such as OpenGL, ImGui, GLFW and GLM. C++ has been preferred because both the language is compiled and the interface is embedded in the OpenGL library.

It would be useful to briefly mention the functions of the open source libraries used. OpenGL is a visualization library used in many applications around the world. It provides convenience as it provides the user with the opportunity to program a "Graphic Processing Unit" (Eng. Graphics Processing Unit, GPU) and can perform mathematical operations very quickly. Second, ImGui is a user interface library built on OpenGL. Thanks to ImGui, changes can be made quickly in the interface. GLFW is a modern windowing library that allows OpenGL and ImGui to be visualized on the same screen. Finally, matrix and vector operations are optimized in the GLM library. This optimization greatly speeds up operations when using OpenGL, as matrix operations must be used to create any point. The uses of OpenGL, GLFW and ImGui in the interface are given in Figure 4.4.

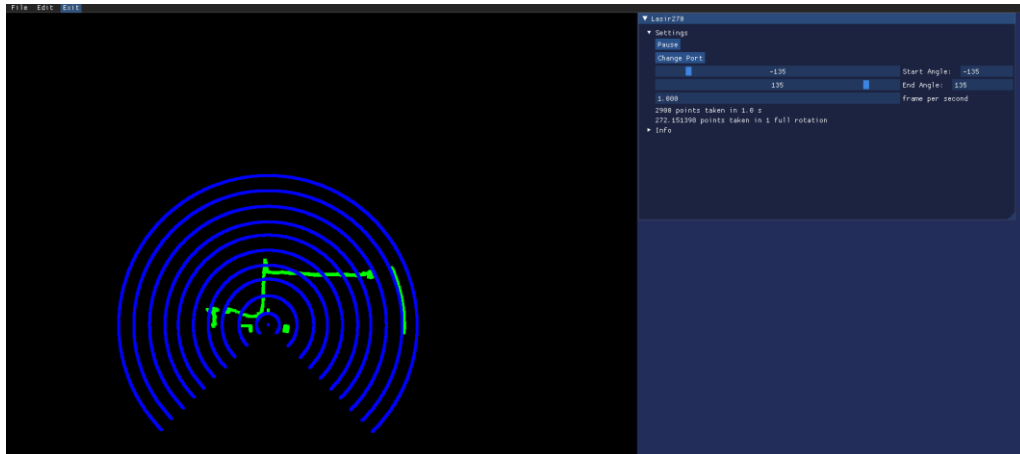


Figure 4.4. Software Interface

CHAPTER 5

TESTING AND ANALYSIS

After the design and integration studies were completed, the testing process was initiated to evaluate the system performance.

5.1 Transmitter Optical Performance

As described in “optical power calculation algorithm” part, as a result of the market research, it was evaluated that three different pulsed wave lasers would be suitable. The tests started with the V1 laser with a peak power of 75 W, and it was decided to continue with a laser with a higher peak power (120 W) and the same optical properties (aperture, beam divergence, etc.) since there was a problem in its supply.

The selected pulsed laser was driven with the development board, the visual of which is given in Figure 5.1. The development board made it possible to set different repetition rate, operating voltage, and pulse width values. Photodiode power sensor, known to measure average power, was used to measure output power in the tests.

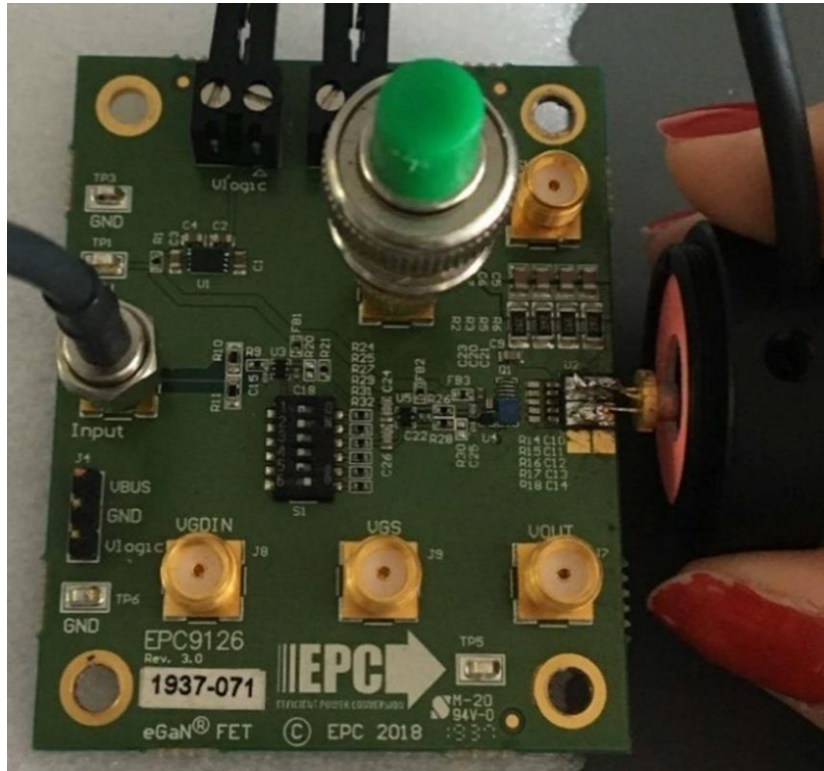


Figure 5.1. Transmitter PCB

First, the variation of the average output power with respect to repetition rate was investigated. In this controlled test, the repetition rate and average output power values measured by selecting the operating voltage of 50 V and a pulse width of 100 ns are given in Table 1.

Table 5.1 Repetition Rate– Average Output Power

Repetition Rate (kHz)	Average Output Power (mW)
5	6.85
10	15.56
20	28.77
30	42.82
40	55.65
50	70.70

When the table is examined, it is seen that as the repetition rate increases, the average output power of the laser increases accordingly. This test was repeated for various operating voltages and then various pulse widths to obtain the graphs in Figure 5.2 and Figure 5.3.

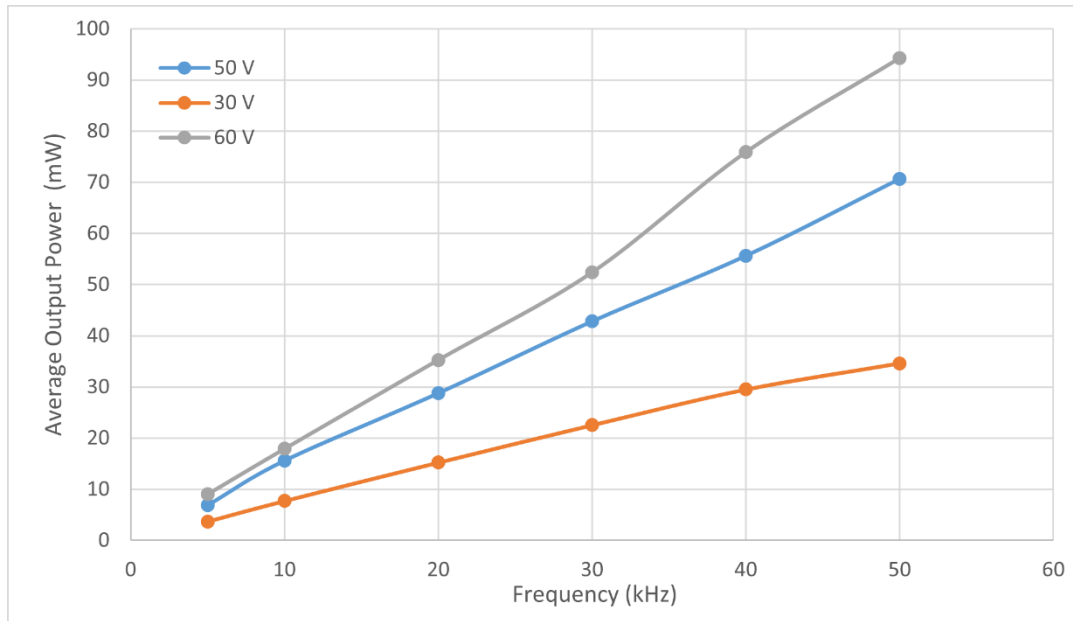


Figure 5.2. Average Output Power – Repetition Rate Graph

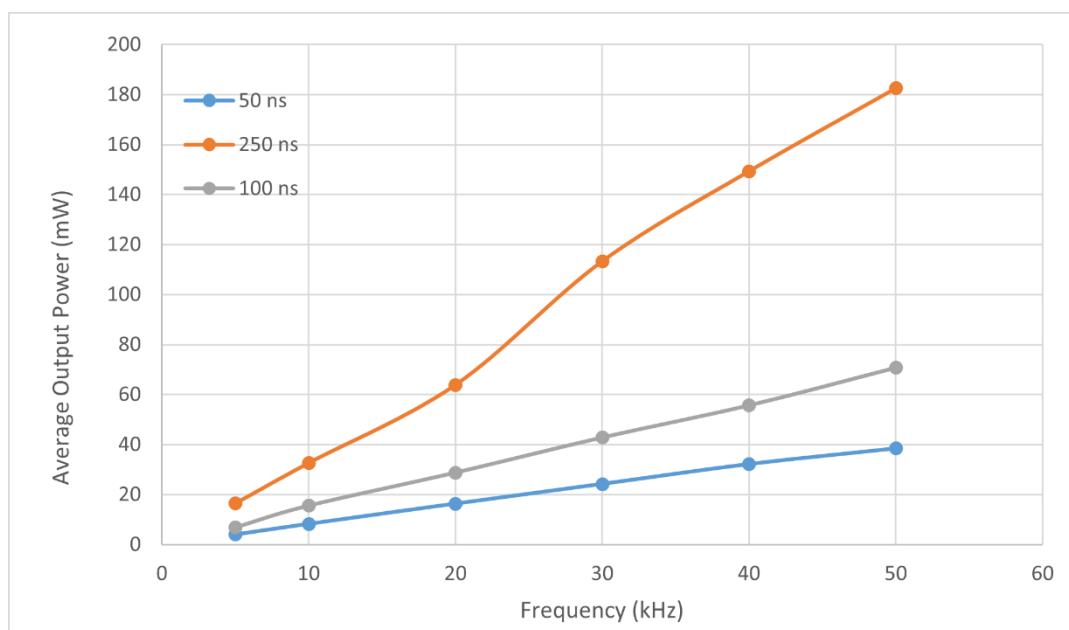


Figure 5.3. Average Output Power – Repetition Rate Graph

Figures shows the repetition rate dependent variation of the average power for various operating voltages and various pulse widths. When the graphs are examined, it is seen that the average output power increases linearly with the frequency, independent of the operating voltage and pulse width.

Secondly, cases where the operating voltage is variable are examined. It is necessary to measure the average output power of the laser at different operating currents. This test could not be performed because there is a current limitation in the transmitter electronic board. The test was carried out at different operating voltages by increasing the highest current that the electronic board can output. In this test, the repetition rate was selected as 30 kHz and the pulse width was kept constant by choosing 100 ns, and the operating voltage and average output power values are given in Table 5.2.

Table 5.2 Operating Voltage – Average Output Power

Operating Voltage (V)	Average Output Power (mW)
30	22.53
40	32.68
50	42.82
60	52.40

When the table is examined, it is seen that as the operating voltage increases, the average output power of the laser increases accordingly. This test was performed with various pulse widths followed by various repetition rate values. Outputs are given in Figure 5.4 and Figure 5.5.

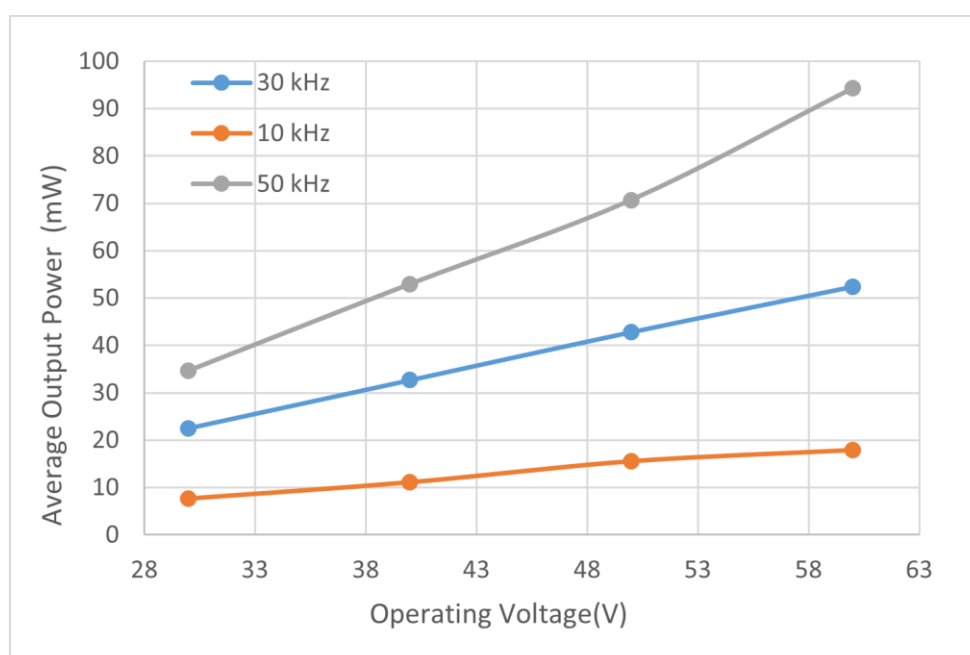


Figure 5.4. Average Output Power – Operating Voltage Graph

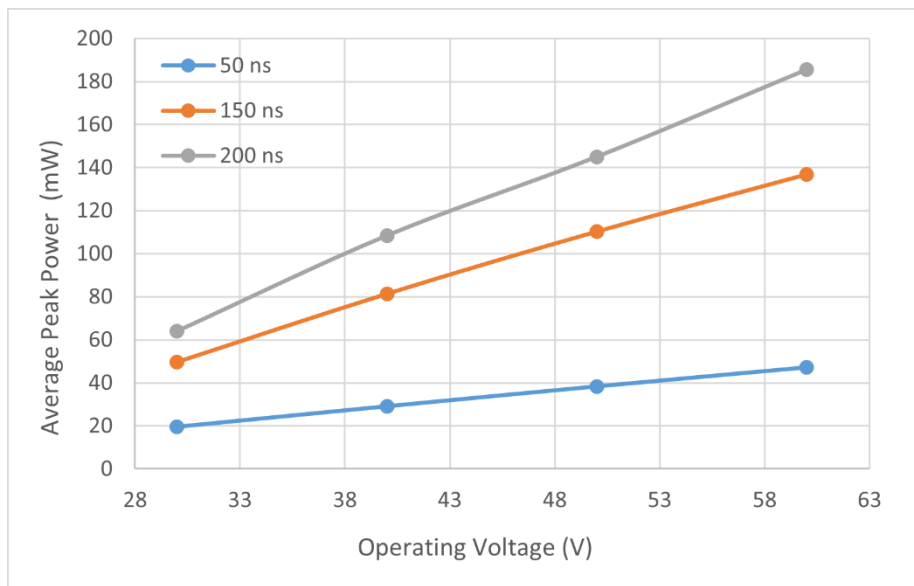


Figure 5.5. Average Output Power – Operating Voltage Graph

Figure shows the variation of average power with operating voltage for various repetition rates and various pulse widths. When the graphs are examined, it is seen that the average output power increases linearly with the operating frequency, independent of the repetition rate and pulse width. Finally, the cases where the pulse width is kept variable by choosing a repetition rate of 30 kHz and an operating voltage of 50 V are discussed. The results are given in Table 5.3.

Table 5.3 Pulse Width – Average Output Power

Pulse Width (ns)	Average Output Power (mW)
50	24.18
100	42.82
150	59.37
200	90.90
250	113.3

In this case, it is seen that the average output power of the laser increases as the operating voltage increases. This test was repeated with various operating voltages followed by various repetition rates. Result graphs are given in Figure 5.6 and Figure 5.7.

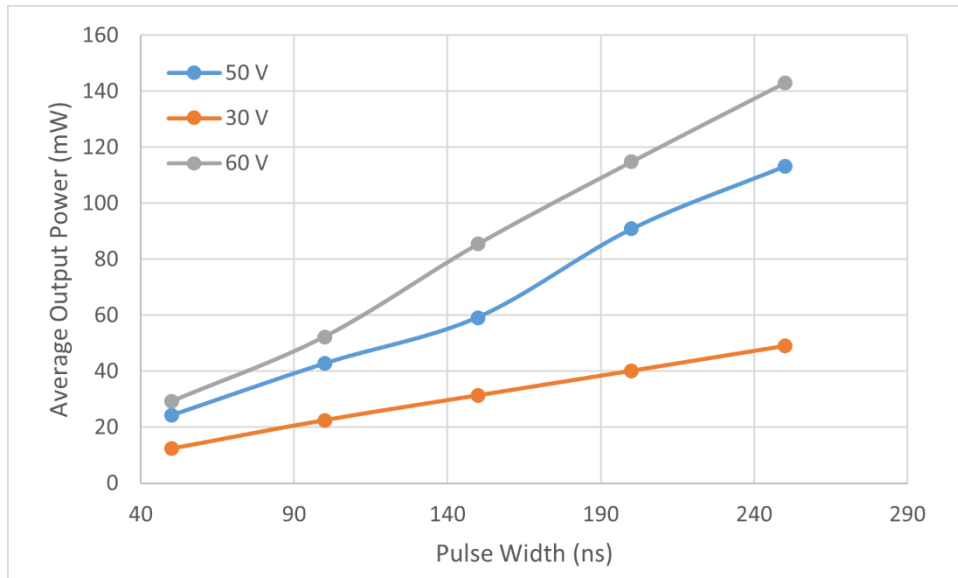


Figure 5.6. Average Output Power – Pulse Width Graph

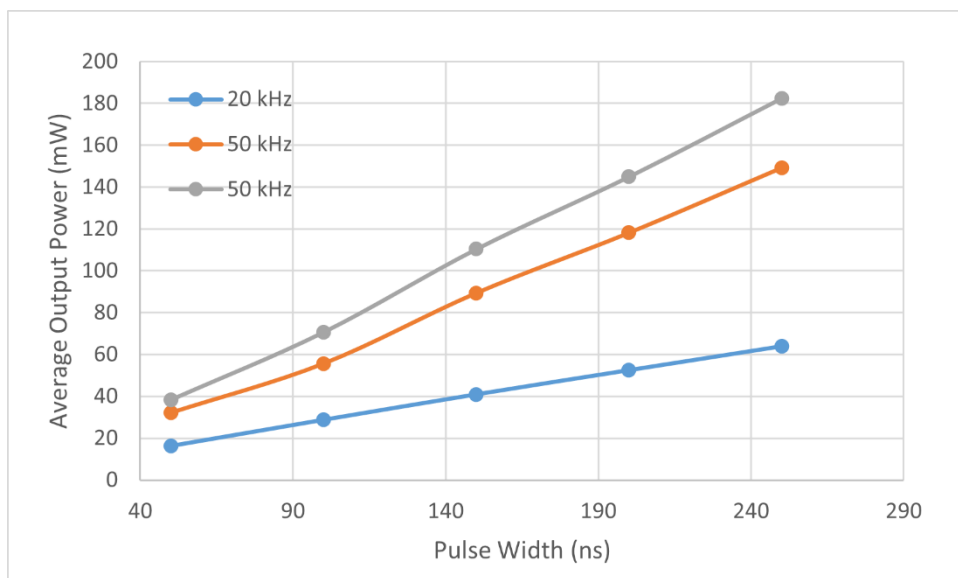


Figure 5.7. Average Output Power – Pulse Width Graph

When Figure is examined, it is seen that the average output power of the transmitter is linearly related to all three variables.

5.1.1 Optical Components Effects on Power

As detailed in the optical design section, two cylindrical lenses are used as the transmitter optics. In addition to these, there is a window that separates the scanning mechanism from the outside environment and acts as a filter. After the laser beams exit the source, they interact with the first lens, the second lens and the window, respectively. The test setup is given in Figure 5.8.

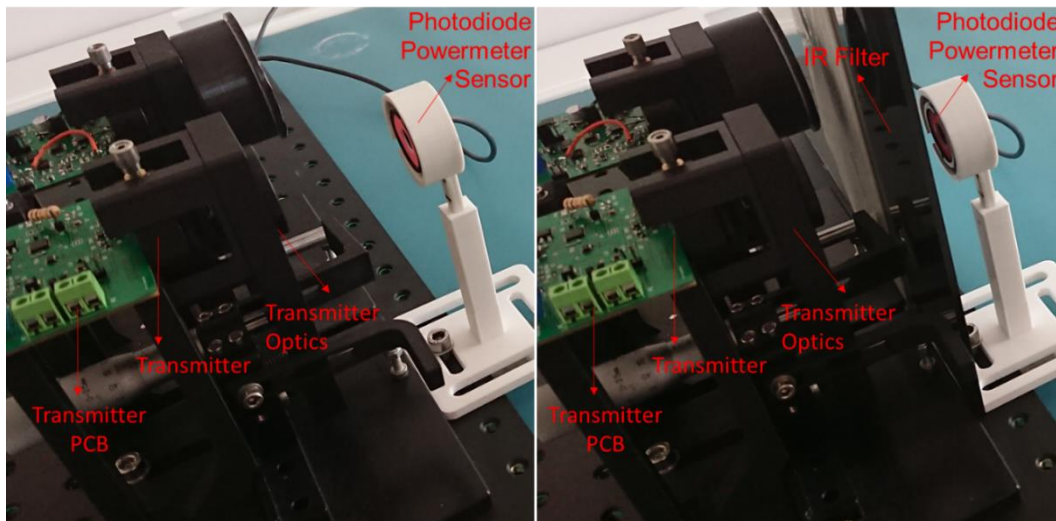


Figure 5.8. Set – Up for Output Power

When Figure 5.8 is examined, only the effect of the transmitter lenses on the left and the effect of the transmitter lenses and the window on the right are examined together. In this test, the laser was performed with a repetition rate of 5 kHz, an operating voltage of 35 V, and a pulse width of 250 ns. Only the average output power values of laser, laser + lens and laser + lens + window configurations were measured and the obtained values are given in Table 5.4.

Table 5.4 Effect of Optical Components on Output Power

	Average Output Power (mW)	Attenuation (%)
Laser	10.43	-
Laser + Lenses	7.83	24.9
Laser + Lenses + Window	6.81	34.7

When the table is examined, it is seen that the lenses reduce the average output power of the laser by about 25% and the window by 10%. Please note that 25% decrease particularly high attenuation. Because the beam divergence of the laser is so wide, some of it is scattered before it reaches the lens. In the case where only the output power of the laser is measured, since the photodiode is placed almost at the output of the laser, all of the rays are collected. As a result of this test, it was seen that the window effect coincides with the transmittance values given in the data sheet.

5.1.2 Beam Divergence, Profile

In this test, the spot diameter was measured at different distances to calculate the beam divergence of the transmitter. The test setup in which the spot diameter was measured is given in Figure 5.9.

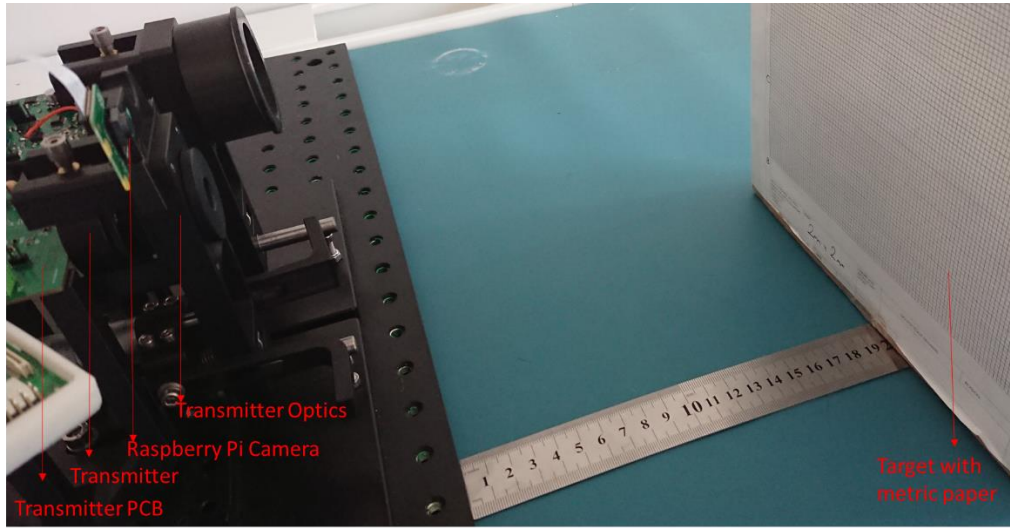


Figure 5.9. Set – Up for Beam Divergence

As seen in the figure, set up consist of transmitter pcb, transmitter, optics, Raspberry Pi camera, metric paper coated target and a ruler to measure the target distance. Light beam coming out of the transmitter were dropped on the target and the image was taken with the help of the camera. Spot diameters were calculated by processing images at different distances. The sample spot image is given in the Figure 5.10.

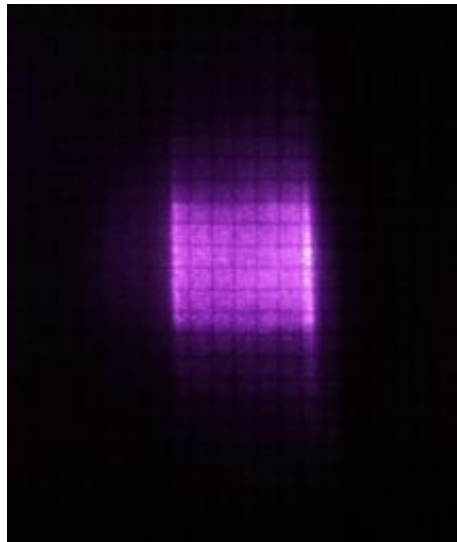


Figure 5.10. Spot Sample

Spot as defined as the area formed by pixels equal to or brighter than half the luminance of the brightest cell. After the horizontal and vertical diameters of this area were found in cell type, the radii were converted to mm.

The best fit line of these data is plotted is given in the Figure 5.11.

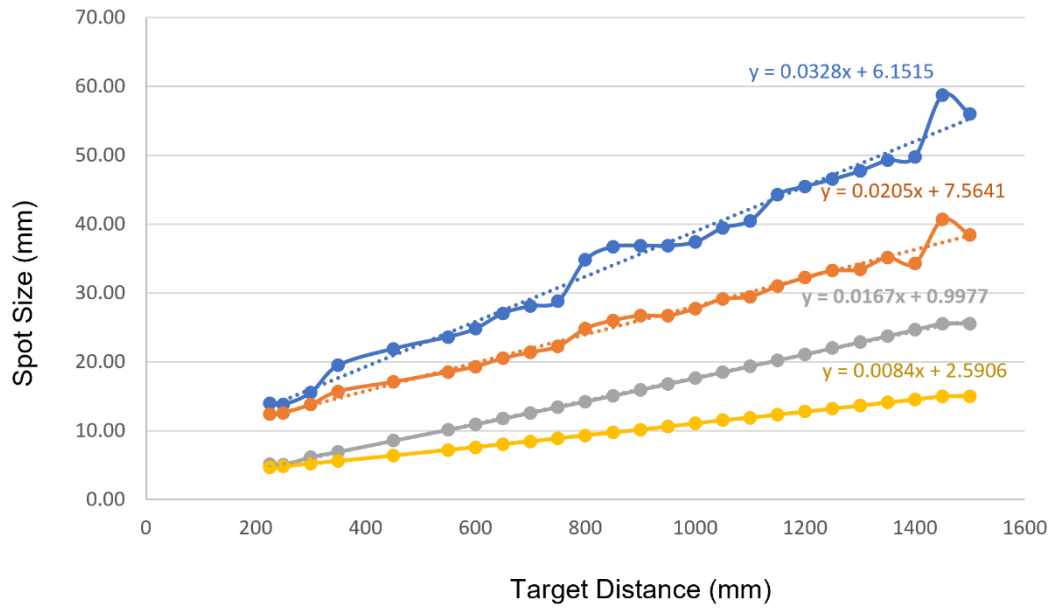


Figure 5.11. Spot Size – Target Distance Graph

In the graph, blue line represents the horizontal spot size, orange line represents the vertical spot size taken from the test. Grey line and yellow line are horizontal spot size and vertical spot size respectively taken from the optical design software.

When the graph is examined, it is seen that the horizontal and vertical spot diameters increase as the distance increases. Since this increase is expected to be linear, the best fit line was drawn. By taking the arctan values of these slopes, the beam divergences were calculated.

The beam divergence values calculated from the test and the optical design software image data are given in the table.

Table 5.5 Beam Divergence Results

	Mrad		Degree	
	Test	Optical Design Software	Test	Optical Design Software
Horizontal Spot	32.76	16.70	1.88	0.96
Vertical Spot	20.53	8.44	1.18	0.48

5.2 Back Focal Length

As in all optical systems, precise positioning of the light sensor and optical elements is important in this system. If the photosensor active surface is not placed in the focus of the receiver optics, the light may not reach the receiver or may not trigger the active surface because they do not come at the right angle. This situation causes the receiver to not be able to generate enough signal and therefore not to be able to measure correctly. In order to avoid these problems, the receiver back focal length (BFL) should be determined. The test setup is given in Figure 5.12.

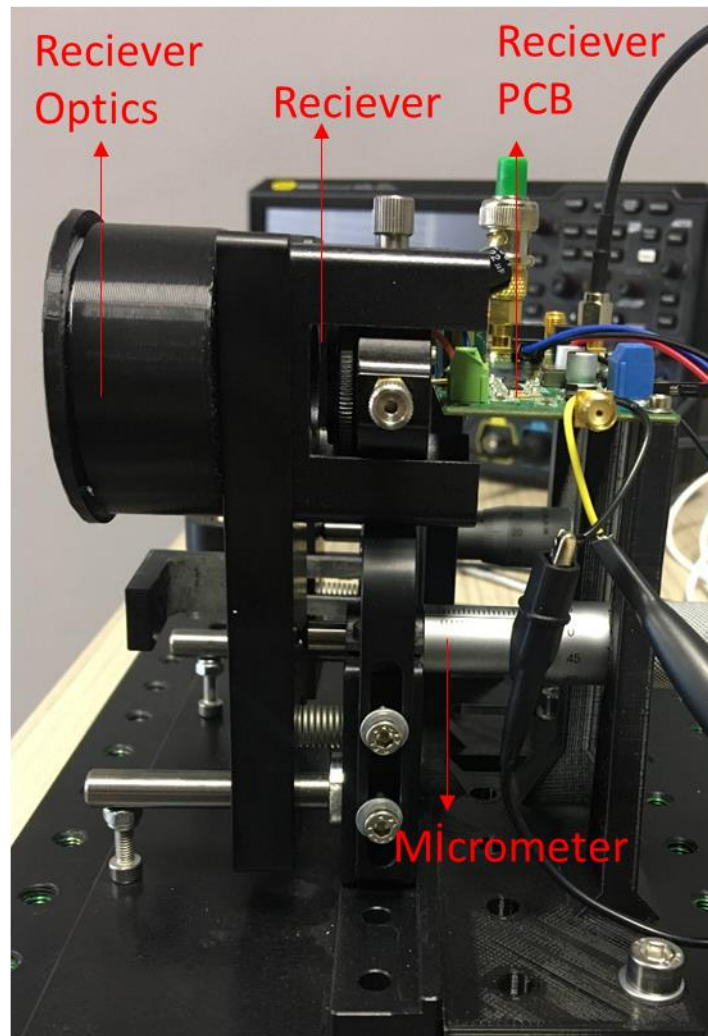


Figure 5.12. BFL Set - Up

As seen in the figure, the set up consist of receiver PCB, receiver, receiver optics and micrometer. The receiver optic can be moved precisely with the micrometer. In this test, the effect of micrometer movement on the receiver signal was investigated by placing the target at different distances. The data in the table are the average signal values received from the receiver in mV.

First, the target was placed at a distance and then the receiver back focal length was increased sensitively starting from 22,12 mm, and the size of the receiver signal was measured with an oscilloscope. The graph of these data is given in Figure 5.13.

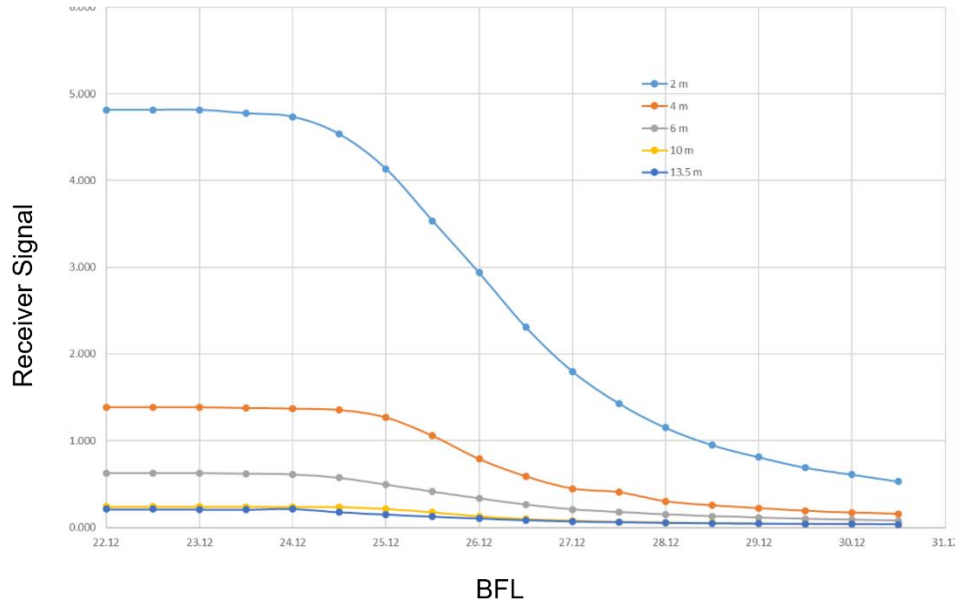


Figure 5.13. Back Focal Length – Receiver Signal Graph

When the figure is examined, it is seen that the receiver signal decreases significantly when the back focal length is above 23.5 mm, regardless of the target distance. As a result of this test, it was evaluated that the ideal receiver back focal length should be between 22.12 and 23.12, and input was provided to the integration process.

5.3 Receiver Performance

In LIDAR systems, the power of the beam reflected from the target varies depending on the distance. The signal strength generated at the receiver decreases with the square of the distance. To confirm this information, a distance dependent receiver signal test was performed. The test setup is given in Figure 5.14.

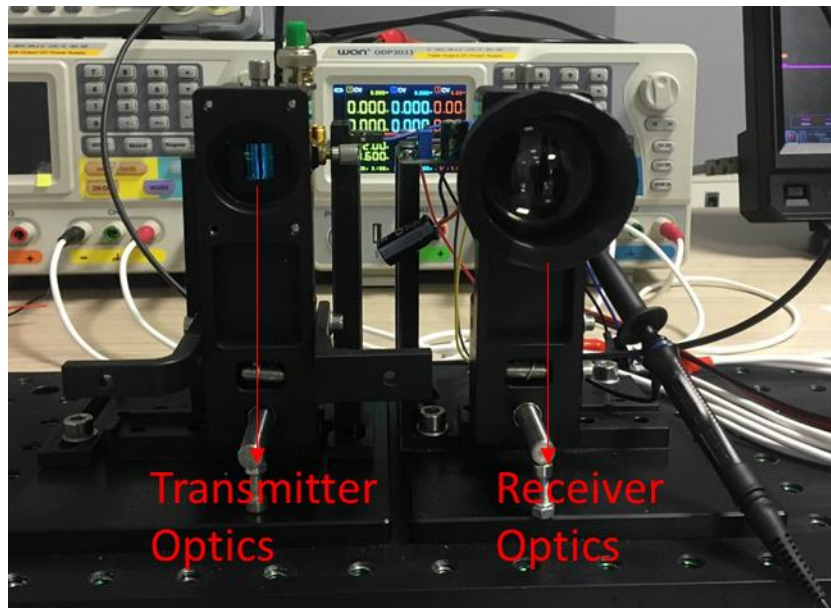


Figure 5.14. Electronic Signal Set-up

A sufficiently large target was used during the test. This test was repeated by adding a window and the effect of the window on the receiver signal was determined.

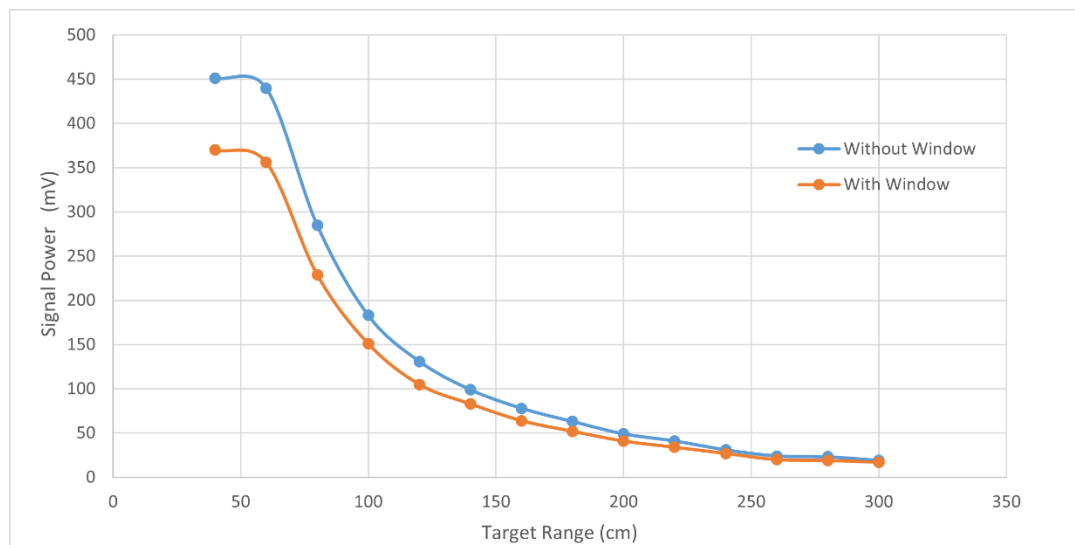


Figure 5.15. Signal Power – Target Range Graph

Regardless of the window, the receiver signal had an inverse square relationship with distance, as expected. It has been observed that the average signal power loss is 16.89% when a window is added to the system.

CHAPTER 6

CONCLUSION

LIDARs have a wide range of applications thanks to advances in laser technology, including obstacle identification, road environment monitoring, atmospheric remote sensing and meteorology, speed measures, and proximity detection. LIDARs have become more small and inexpensive thanks to advances in semiconductor laser and photodetector technology. However, there is definitely room for development, particularly in terms of system architecture. Optical, mechanical, optomechanical design, and software development are all required for the construction of an LIDAR.

The LIDAR obtained in this study was successfully integrated and operated. As mentioned in the test chapter, obstacle detection up to 13 meters in indoor area has been successfully performed. Since the measurement resolution of the electronic circuit is 3 cm, the tests were measured with an accuracy of 6 cm. After that, outdoor tests were carried out and obstacle detection was carried out successfully.

Laser power calculations made in this study are an important topic. In particular, very detailed calculations were made on the intersection area of the target and the laser spot. Identifying these intersection areas is important to determine the optical power coming into the receiver. Optical power reaching the receiver affects the resolution and detectivity performance. If the power reaching the receiver remains below a certain level, it will not trigger the receiver. In this case, the signal cannot be received from the target and the object cannot be detected.

The range of the LIDAR varies according to the reflection coefficients of the targets. The range of the LIDAR obtained in this study is 50 m at 10% reflectivity and up to 110 meters at 90% reflectivity. In this study, a laser with 120 mW pulse output power was used. The maximum range of the LIDAR can be increased by using a higher power laser.

Commercial optical system design software was used to simulate the laser diode based on its astigmatic properties. Thanks to custom-designed cylindrical lens pairs, divergence angles of 1.88° and 1.18° were attained. A circular beam could not be obtained because the aperture of the diode is rectangular. Larger budgets and more complex optical components are needed to achieve smaller beam divergence.

This product can be used in many areas. It can be used in people and product counting, autonomous devices, especially in the fields of industrial safety. In addition, this product can work integrated with cameras.

Point cloud data was created by running LIDAR, whose prototype was completed, in an office environment where there are different obstacles such as people, board, plants and walls. The related image is given in Figure 6.1



Figure 6.1. Test Image

The architectural drawing and the generated point cloud data are given in the Figure 6.2 and Figure 6.3 respectively.

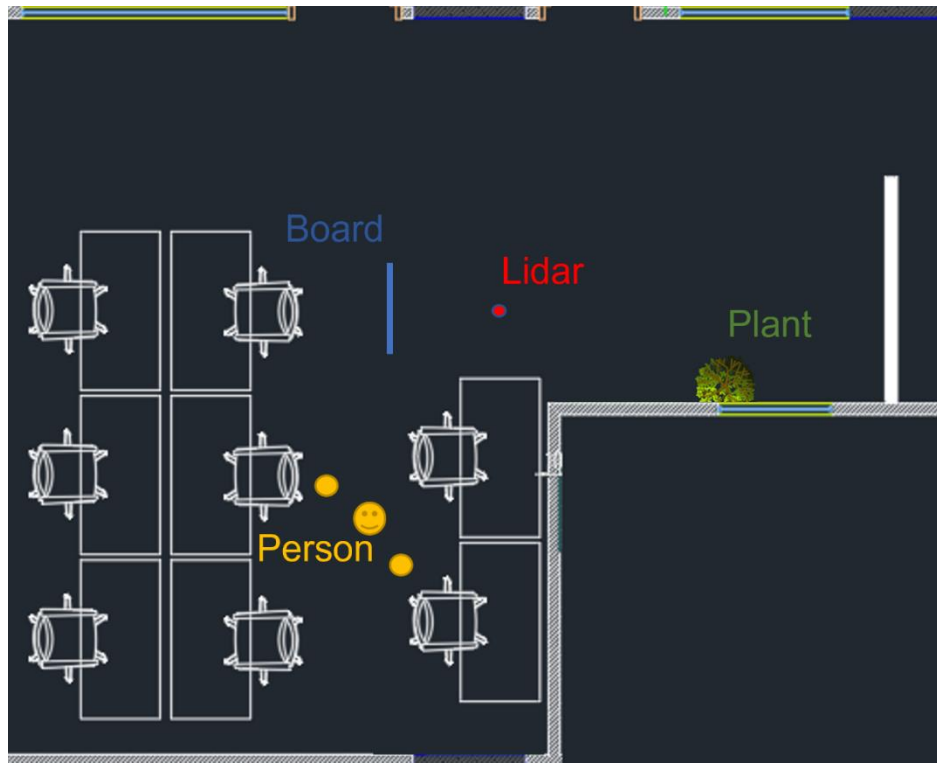


Figure 6.2. The Architectural Drawing

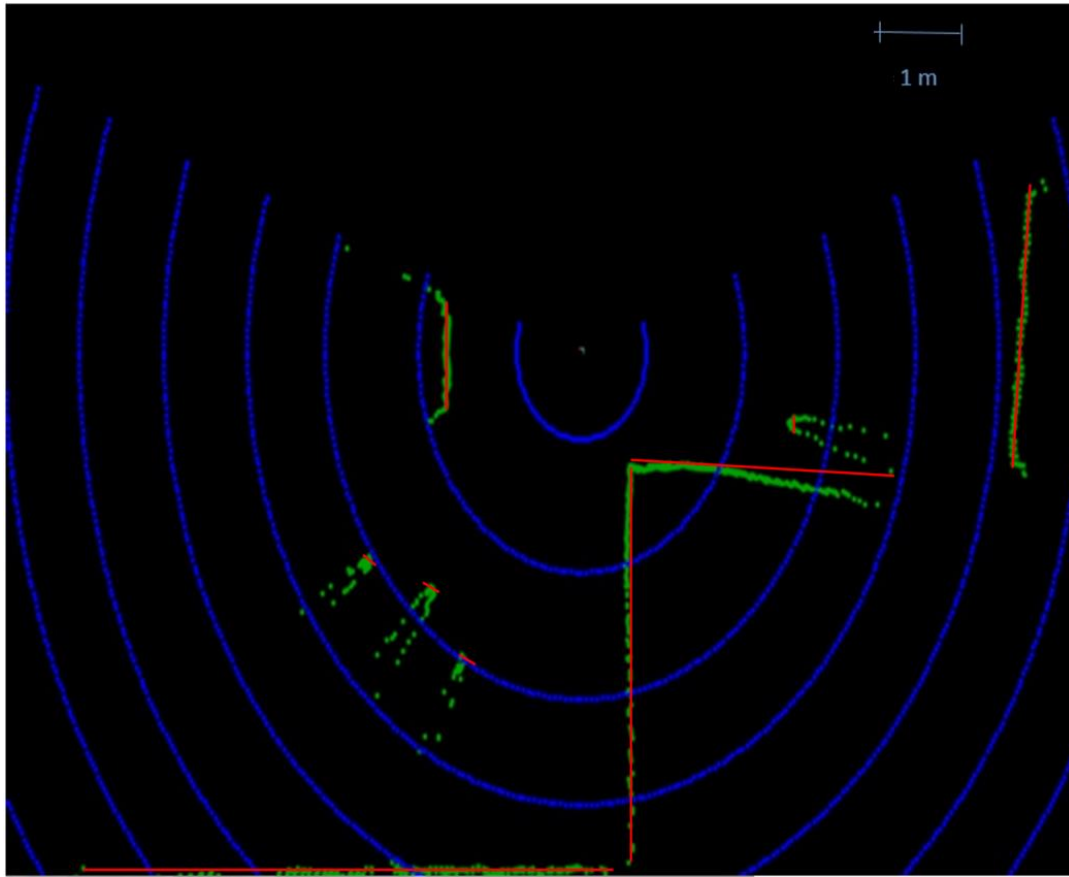


Figure 6.3. The Point Cloud Data

In the Figure 6.3, LIDAR is at the center of the point cloud data. The red lines in the picture show the actual distance data of the objects. There are some differences between the actual distances of the objects and the LIDAR data. The reason for this difference; Some of the beams emanating from the laser reach the target earlier. Since these rays return to the receiver earlier, these rays dominate. Therefore, there may be differences in the position measurements of the objects.

The image of the LIDAR that developed in this work is shown in Figure 6.4. Technical datasheet is given in the Appendix A.



Figure 6.4. The Image of LIDAR

APPENDICES

A. DATASHEET

Laser Class	1 (EC 60825-1:2014)
Laser	IR (905 nm)
Min. Operating Range	4 m
Max. Operating Range	50 m (@ %10 Reflection) 110 m (@ %90 Reflection)
Field of View	270° (Adjustable)
Heater	25 W
Interface	TCP/IP and RS 485
Enclosure Rating	IP 67 (TS 3033 EN 60529)
Protection Class	III (EN 50178 (1997,10))
Amb. Opt. Temperature	-40°C ~ +60°C
Operating Voltage	12 VDC
Weight	550 g
False Alarm Prevention	Fog. Rain, Snow Correction Atmospheric Filtration Background Learning Pollution warning

REFERENCES

- [1] G., Goyer G.; R., Watson, "The Laser and its Application to Meteorology," *Bulletin of the American Meteorological Society*, vol. 9, no. 44, pp. 564-570, 1963.
- [2] Lin S.; Cong, L ; Liangfu, C, "LIDAR," in *International Encyclopedia of Geography: People, the Earth, Environment and Technology*, Wiley - Blackwell: Oxford,UK, 2016, pp. 1-9.
- [3] Weiss, U.; Biber, P.; Laible, S.; Bohlmann, K.; Zell, A., "Plant Species Classification Using a 3D LIDAR Sensor and Machine Learning," *Proceedings of the 2010 Ninth International Conference on Machine Learning and Applications*, pp. 339-345, 2010.
- [4] Wang D; Watkins C; Xie H, "MEMS Mirror for LiDAR: A Review," *micromachines*, 2020.
- [5] Henning,S. ; Ippolito, C. A. ; Krishnakumar, K.; Stephanyan, V.; Teodorescu, M., "3D LiDAR SLAM Integration with GPS/INS for UAVs," *Urban GPS-Degraded Environments*, p. 448, 2017.
- [6] Maturana, D.; Scherer, S. VoxNet, "A 3D Convolutional Neural Network for Real Time Object Recognition," in *Proceeding of the 2015 IEEE/RSJ International Conference on Intelligent Robots and Systems (IROS)*, Hamburg,Germany, 2015.
- [7] Miyasaka, T.; Ohama, Y.; Ninomiya, Y., "Ego-motion estimation and moving object tracking using multilayer LIDAR," *Proceedings of the 2009 IEEE intelligent vehicles symposium* , pp. 151-156, 2009.

- [8] M. C. Amann, T. Bosch, M. Lescure, R. Myllyla, M. Rioux, "Laser ranging: A critical review of usual techniques for distance measurement," *Optical Engineering*, vol. 1, no. 40, pp. 10-19, 2001.
- [9] G. Berkovic, E. Shafir, "Optical Methods for distance and displacement measurements," *Advances in Optics and Photonics* , vol. 4, pp. 441-471, 2012.
- [10] Sun B., Li B., "A Rapid Method to Achieve Aero-Engine Blade Form Detection," *Sensors*, no. 15, 2015.
- [11] M. C. Amann, T. Bocsh, M. Lescure, R. Myllyla, M. Rioux, "Laser Ranging: A critical review of usual techniques for distance measurement," *Optical Engineering*, vol. 1, no. 40, pp. 10-19, 2001.
- [12] [Online]. Available: <https://www.avsystem.com/blog/time-of-flight/#:~:text=The%20time%2Dof%2Dflight%20principle,that%20object%20from%20the%20source..>
- [13] [Online]. Available: <https://medium.com/playment/a-primer-on-lidar-for-autonomous-vehicles-efa04ab72a94>.
- [14] Gelbart A., Redman B. C., Light R. S., Schwartzlow C. A., Gri A. J., "Flash LIDAR based on multiple-slit streak tube imaging LIDAR," *Laser Radar Technology and Applications* , pp. 9-18, 2002.
- [15] P. A., "How Multi-Beam Flash LIDAR Works," [Online]. Available: <https://ouster.com/blog/how-multi-beamflash->. [Accessed 2021].
- [16] Liu J., Sun Q., Fan Z., Jia Y., , "TOF LIDAR Development in Autonomous Vehicle," *IEEE 3rd Optoelectronics Global Conference* , pp. 185-190, 2018.

- [17] Kim G., Park Y., "LIDAR pulse coding for high resolution range imaging at improved refresh rate," *Opt. Express*, 2016.
- [18] Wight D. R., Heaton J. M., Hughes B. T., Birbeck J. C. H., Hilton K. P., Taylor D. J., "Novel phased array optical scanning device implemented using GaAs7AlGaAs technology," *Applied Physics*, no. 59, pp. 899-901, 1991.
- [19] MCManamon P., Dorschner T., Corkum D., Friedman L., Hobbs D., Holz M., Liberman S., Resler D. Sharp R., Watson E., , "Optical phased array technology," *IEEE*, no. 84, pp. 268-298, 1996.
- [20] Halterman R., Bruch M., , "Velodyne HDL-64E LIDAR for unmanned surface vehicle obstacles detection," *SPIE Def. Secur. Sens.*, 2010.
- [21] Nikolas, "Airborne LIDAR : Hoe Does it Work," *Airborne Research* , 2006.
- [22] Frank L. Pedrotti, Leno M. Pedrotti, Leno S. Pedrotti , Introduction to Optics.
- [23] V. N. Mahajan, Aberration Theory Made Simple, 1991.
- [24] Sahapong Kruapech, Joewono Widjaja, "Laser Range Finder Using Gaussian Beam Range Equation," *Optics & Laser Technology*, 2009.
- [25] Sabatini R., Richardson M., "Airborne Laser Systems Testing and Analysis," *Flight Test Techniques Series*, no. 26.
- [26] L. B. Wolff, "Relative brightness of specular and diffuse reflection," *Optical Engineering*, 1994.
- [27] A. A. A.-. Tedemy, "The Development of a 3D LADAR Simulator Based on a Fast Target Impulse Response Generation Approach," 2017.

- [28] Richmond R., Cain S. C., Direct - Detection LADAR Systems, SPIE, 2009.
- [29] Sorin Pohoata, Nicolae Dumitru Alexandru, Adrian Popa, "An Approximation of Gaussian Pulses".
- [30] Huang Z., Zimmer M., Hepp S., Jetter M., Michler P., "Optical Gain and Lasing Properties of InP/AlGaInP Quantum Dot Laser Diode Emitting at 660 nm," *IEEE Journal of Selected Topics in Quantum Electronics*, 2019.
- [31] [Online]. Available:
<https://www.techbriefs.com/component/content/article/tb/supplements/pit/features/articles/37187>.
- [32] R. Michalzik, Fundamentals, Technology and Applications of Vertical Cavity Surface Emitting Lasers, Springer, 2013.
- [33] J. Skidmore, "Semiconductor lasers for 3D Sensing," *Optics and Photonics News*, 2019.
- [34] W. L. Wolfe, "Atmospheric Transmission and Radiation," in *Introduction to Infrared System Design* , SPIE, 1996.
- [35] Roberto Sabatini, Mark Anthony Richardson, "New Techniques for laser beam atmospheric extinction measurement from manned and unmanned aerospace vehicles," *Optical Engineering*.
- [36] K. A. Fuler, "Scattering and Absorption Cross Sections of Compound Spheres," *Journal of the Optical Society of America* .
- [37] Diogo A.R. Lopes, Antonio Ramires Fernandes, "Atmospheric Scattering," in *Encontro Portuges de Computação Grafica*, 2014.

- [38] Elder T., Strong J., "The Infrared Transmission of Atmospheric Windows," pp. 255-189.
- [39] Kneizys F. X., Shuttle, E. P., Abreau L. W., Chetwynd J. H., Anderson G. P., Gallery W. O., Selby J.E.A., Clough S.A., *Users Guide to LOWTRAN 7*, 1988.
- [40] Bram van Ginneken, Marigo Stavridi, Jan J. Koenderink, "Diffuse and Specular Reflectance from Rough Surfaces," *Applied Optics*, 1998.
- [41] F. Stoliker, G. Bever, Introduction to Flight Test Engineering, 2005.
- [42] [Online]. Available: <https://www.osioptoelectronics.com/application-notes/an-photodiode-parameters-characteristics.pdf>.
- [43] Verena Mackowiak, Jens peupelmann, Yi Ma, Anthony Gorges, "NEP-Noise Equivalent Power," [Online]. Available: https://www.thorlabs.com/images/TabImages/Noise_Equivalent_Power_White_Paper.pdf.
- [44] P. L. Richards, "Bolometers for infrared and millimeter waves," *Journal of Applied Physics*, no. 76, 1994.
- [45] [Online]. Available: <http://www.osioptoelectronics.com/application-notes/AN-Photodiode-Parameters-Characteristics.pdf>.
- [46] Friedrich Bachmann, Peter Loosen, Reinhart Poprawe, High Power Diode Lasers Tehcnology and Applications.
- [47] "<https://blog.rpmclasers.com/laser-diode-fundamentals-beam-properties>," [Online].
- [48] J.W.Foreman, "Computation of RMS Spot Radii by Ray Tracing," *Applied Optics*.

- [49] [Online]. Available:
https://www.thorlabs.com/newgrouppage9.cfm?objectgroup_ID=7.
- [50] Amann M., Lescure T., Myllyla R., Rioux M., "Laser ranging: a critical review of usual techniques for distance measurement," *Optical Engineering*, 2001.